The Journal of Chemical Physics

Classical Wigner model based on a Feynman path integral open polymer

Cite as: J. Chem. Phys. **152**, 094111 (2020); https://doi.org/10.1063/1.5126183
Submitted: 06 September 2019 . Accepted: 16 February 2020 . Published Online: 05 March 2020

S. Karl-Mikael Svensson, Jens Aage Poulsen, and Gunnar Nyman

The Journal of Chemical Physics ARTICLE scitation.org/journal/jcp

Classical Wigner model based on a Feynman path integral open polymer

Cite as: J. Chem. Phys. 152, 094111 (2020); doi: 10.1063/1.5126183
Submitted: 6 September 2019 • Accepted: 16 February 2020 •
Published Online: 5 March 2020

S. Karl-Mikael Svensson, Jens Aage Poulsen,[a] and Gunnar Nyman[b]

AFFILIATIONS

Department of Chemistry and Molecular Biology, University of Gothenburg, SE 405 30 Gothenburg, Sweden

[a]Electronic mail: jens.poulsen@gu.se
[b]Author to whom correspondence should be addressed: nyman@chem.gu.se

ABSTRACT

The classical Wigner model is one way to approximate the quantum dynamics of atomic nuclei. Here, a new method is presented for sampling the initial quantum mechanical distribution that is required in the classical Wigner model. The new method is tested for the position, position-squared, momentum, and momentum-squared autocorrelation functions for a one-dimensional quartic oscillator and double well potential as well as a quartic oscillator coupled to harmonic baths of different sizes. Two versions of the new method are tested and shown to possibly be useful. Both versions always converge toward the classical Wigner limit. For the one-dimensional cases, some results that are essentially converged to the classical Wigner limit are acquired and others are not far off. For the multi-dimensional systems, the convergence is slower, but approximating the sampling of the harmonic bath with classical mechanics was found to greatly improve the numerical performance. For the double well, the new method is noticeably better than the Feynman–Kleinert linearized path integral method at reproducing the exact classical Wigner results, but they are equally good at reproducing exact quantum mechanics. The new method is suggested as being interesting for future tests on other correlation functions and systems.

I. INTRODUCTION

When studying molecular systems computationally, a problem that can arise is how to account for the quantum mechanical behavior of the atomic nuclei without having to solve the time dependent Schrödinger equation using wavefunctions and, instead, work with, e.g., trajectories, which has the potential to be significantly cheaper computationally for many chemically interesting problems. Several different methods exist, which can be used to address this problem, such as centroid molecular dynamics (CMD)[1] that has been well explained by Jang and Voth,[2] ring polymer molecular dynamics (RPMD),[3] semi-classical initial value representation (SC-IVR)[4] that has been well explained by Miller,[5] Matsubara dynamics,[6] and the classical Wigner (CW) method[7,8] [also called linearized semi-classical initial value representation (LSC-IVR), and linearized path integral (LPI)]. A new implementation of the classical Wigner method is the topic of the present article.

The classical Wigner method starts with a quantum mechanical phase space distribution, which is propagated forward in time classically. Finding the initial distribution is typically problematic. In this work, a new way to sample the initial phase space distribution is presented and tested for some simple problems.

The classical Wigner method, CMD, and RPMD can all be seen as approximations to Matsubara dynamics and give worse results than Matsubara dynamics.[6,9] However, for large systems, Matsubara dynamics would be too computationally demanding to be practical.[6]

Comparing CMD and RPMD to the classical Wigner method, one major advantage of the former two is that the quantum mechanical ensemble is conserved during the dynamics, while it is not in the classical Wigner method. On the other hand, for a harmonic oscillator, the classical Wigner method is exact for any correlation function,[7] while CMD can formally be done for non-linear operators,[10] but it is a much more complicated process than for linear operators, and RPMD is only exact for correlation functions where at least one operator is linear.[3]

The classical Wigner method can be seen as an approximation of the semi-classical initial value representation. In this approximation, quantum real time coherence is, however, lost, which may not be very important in large or condensed phase systems since these

typically decohere rapidly.[11] An advantage with the approximation is less oscillatory integrands to handle numerically.[11]

From the above comparisons, it can be seen that one of the reasons for using the classical Wigner method is that it may better handle non-linear correlation functions at a reasonable expense of computational resources, compared to the other available methods.

In the new implementation of the classical Wigner method that is presented in this paper, the initial phase space distribution is sampled with an imaginary time path integral polymer similar to those that can be found in CMD and RPMD, but in those cases, these polymers are closed rings and in the present implementation of the classical Wigner method, the polymer has an opening. The open polymer presented here is more closely related to those that can be found in the work of Bose and Makri[12] and Bonella *et al.*[13,14]

In what follows, first, the classical Wigner method is explained (Sec. II), and a new path integral open polymer implementation of it is presented (Sec. III). After that, the computational details (Sec. IV) and the results (Sec. V) are presented, and conclusions (Sec. VI) are drawn.

II. CLASSICAL WIGNER METHOD

The classical Wigner method was in its first form introduced, but not necessarily recommended by Heller.[7] In its current more general form, which is applicable to correlation functions, it was introduced by Wang, Sun, and Miller.[8] The classical Wigner method has as its basis the Wigner phase space distribution.[15,16] In one dimension, easily generalized to any number of dimensions, the Wigner transform is

$$\left(\hat{\Omega}\right)_{\mathrm{W}}[x,p] = \int_{-\infty}^{\infty} \mathrm{d}\eta\, \mathrm{e}^{-i\eta p/\hbar} \left\langle x + \frac{\eta}{2}\middle|\hat{\Omega}\middle|x - \frac{\eta}{2}\right\rangle, \tag{1}$$

where $\hat{\Omega}$ is an arbitrary operator, x is the position, p is the momentum, η is a variable with the dimension of the length, $\hbar$ is the reduced Planck constant, and i is the imaginary unit. The Wigner function is the Wigner transform of the probability density operator $\frac{1}{2\pi\hbar}|\Psi\rangle\langle\Psi|$, where $|\Psi\rangle$ is the ket of the state of the system. This distribution is an exact quantum mechanical quasi-probability distribution and can be used to calculate expectation values,

$$\left\langle\hat{\Omega}\right\rangle = \int_{-\infty}^{\infty} \mathrm{d}x \int_{-\infty}^{\infty} \mathrm{d}p \left(\tfrac{1}{2\pi\hbar}|\Psi\rangle\langle\Psi|\right)_{\mathrm{W}}[x,p]\left(\hat{\Omega}\right)_{\mathrm{W}}[x,p]. \tag{2}$$

The classical Wigner method consists of taking the quantum mechanical transformed quantity and propagating it forward in time with classical mechanics (CM), i.e.,

$$\left(\mathrm{e}^{\frac{i\hat{H}t}{\hbar}}\hat{\Omega}\,\mathrm{e}^{-\frac{i\hat{H}t}{\hbar}}\right)_{\mathrm{W}}[x,p] \simeq \left(\hat{\Omega}\right)_{\mathrm{W}}[x(t),p(t)], \tag{3}$$

where $\hat{H}$ is the Hamiltonian operator and t is time. Thus, the classical Wigner method works by initiating with a quantum mechanical distribution and then propagating it classically, thereby taking account of all equilibrium quantum effects e.g., zero-point energy, but overlooking e.g., dynamic tunneling and quantum interference within the dynamics. The method is exact for potentials up to and including harmonic terms.[7] For a detailed derivation of the classical Wigner method, the review by Liu[17] can be recommended.

The classical Wigner method has been applied successfully to, e.g., calculating the kinetic energy and density fluctuation spectrum in liquid neon[18] and vibrational energy relaxation rate constants,[19,20] but the classical Wigner method has also been found to have limitations for calculating the self-diffusion coefficient of liquid water[21] or handling anisotropic materials.[22]

III. FEYNMAN PATH INTEGRAL OPEN POLYMER

Let us assume that the quantity of interest for a system is the canonical time correlation function,

$$\left\langle\hat{A}\hat{B}(t)\right\rangle = \frac{1}{Z}\,\mathrm{Tr}\left\{\hat{A}\,\mathrm{e}^{-\beta\hat{H}}\,\mathrm{e}^{\frac{i\hat{H}t}{\hbar}}\hat{B}\,\mathrm{e}^{-\frac{i\hat{H}t}{\hbar}}\right\}, \tag{4}$$

where $\hat{A}$ and $\hat{B}$ are arbitrary operators, β is the inverse of Boltzmann's constant times the absolute temperature, Z is the partition function, and Tr denotes a trace. The choice of placing the Boltzmann operator after $\hat{A}$, instead of before, is arbitrary and only determines the sign of the imaginary part of the correlation function, since we have,

$$\frac{1}{Z}\,\mathrm{Tr}\left\{\mathrm{e}^{-\beta\hat{H}}\hat{A}\,\mathrm{e}^{\frac{i\hat{H}t}{\hbar}}\hat{B}\,\mathrm{e}^{-\frac{i\hat{H}t}{\hbar}}\right\} = \frac{1}{Z}\left(\mathrm{Tr}\left\{\hat{A}\,\mathrm{e}^{-\beta\hat{H}}\,\mathrm{e}^{\frac{i\hat{H}t}{\hbar}}\hat{B}\,\mathrm{e}^{-\frac{i\hat{H}t}{\hbar}}\right\}\right)^{*}. \tag{5}$$

The trace can be written as an integral over the position, x_1, eigenkets,

$$\left\langle\hat{A}\hat{B}(t)\right\rangle = \frac{1}{Z}\int_{-\infty}^{\infty}\mathrm{d}x_1\left\langle x_1\middle|\hat{A}\,\mathrm{e}^{-\beta\hat{H}}\,\mathrm{e}^{\frac{i\hat{H}t}{\hbar}}\hat{B}\,\mathrm{e}^{-\frac{i\hat{H}t}{\hbar}}\middle|x_1\right\rangle. \tag{6}$$

By dividing the Boltzmann operator $\mathrm{e}^{-\beta\hat{H}}$ into N factors $\mathrm{e}^{-\frac{\beta}{N}\hat{H}}$ and inserting $N-1$ identity operators, $\hat{1} = \int_{-\infty}^{\infty}\mathrm{d}x_j\,|x_j\rangle\langle x_j|$, the correlation function can be written as

$$\begin{aligned}\left\langle\hat{A}\hat{B}(t)\right\rangle = \frac{1}{Z}\left\{\prod_{j=1}^{N}\int_{-\infty}^{\infty}\mathrm{d}x_j\right\}&\left\langle x_1\middle|\hat{A}\,\mathrm{e}^{-\frac{\beta}{N}\hat{H}}\middle|x_2\right\rangle\\ &\times\left\langle x_2\middle|\mathrm{e}^{-\frac{\beta}{N}\hat{H}}\middle|x_3\right\rangle\cdots\left\langle x_{N-1}\middle|\mathrm{e}^{-\frac{\beta}{N}\hat{H}}\middle|x_N\right\rangle\\ &\times\left\langle x_N\middle|\mathrm{e}^{-\frac{\beta}{N}\hat{H}}\,\mathrm{e}^{\frac{i\hat{H}t}{\hbar}}\hat{B}\,\mathrm{e}^{-\frac{i\hat{H}t}{\hbar}}\middle|x_1\right\rangle,\end{aligned} \tag{7}$$

which can be recognized as a Feynman path integral[23] in imaginary time ($-i\hbar\beta$), and this in turn can be rewritten as Wigner transforms,

$$\begin{aligned}\left\langle\hat{A}\hat{B}(t)\right\rangle = \frac{1}{Z}\left\{\prod_{j=1}^{N}\int_{-\infty}^{\infty}\int_{-\infty}^{\infty}\frac{\mathrm{d}x_j\,\mathrm{d}p_j}{2\pi\hbar}\right\}&\mathrm{e}^{-\frac{i}{\hbar}\sum_{j=1}^{N}p_j\left(x_{j+1}-x_j\right)}\\ &\times\left(\hat{A}\,\mathrm{e}^{-\frac{\beta}{N}\hat{H}}\right)_{\mathrm{W}}\left[\frac{x_1+x_2}{2},p_1\right]\left(\mathrm{e}^{-\frac{\beta}{N}\hat{H}}\right)_{\mathrm{W}}\left[\frac{x_2+x_3}{2},p_2\right]\\ &\cdots\left(\mathrm{e}^{-\frac{\beta}{N}\hat{H}}\right)_{\mathrm{W}}\left[\frac{x_{N-1}+x_N}{2},p_{N-1}\right]\\ &\times\left(\mathrm{e}^{-\frac{\beta}{N}\hat{H}}\,\mathrm{e}^{\frac{i\hat{H}t}{\hbar}}\hat{B}\,\mathrm{e}^{-\frac{i\hat{H}t}{\hbar}}\right)_{\mathrm{W}}\left[\frac{x_N+x_1}{2},p_N\right],\end{aligned} \tag{8}$$

where $x_{N+1} = x_1$ so that the coordinates make a loop.

If $\frac{\beta}{N}$ is approaching 0 and only finite temperatures are of interest, i.e., N is approaching infinity, then the Wigner transform of the Boltzmann operator is simply the classical Boltzmann factor. In this same limit, the Boltzmann operators can be separated from the transforms involving $\hat{A}$ and $\hat{B}$ and thus make up their own Wigner transforms, without consequence,

$$\begin{aligned}\left\langle \hat{A}\hat{B}(t)\right\rangle = \lim_{N\to\infty}\frac{1}{Z}\left\{\prod_{j=1}^{N}\int_{-\infty}^{\infty}\int_{-\infty}^{\infty}\frac{\mathrm{d}x_j\,\mathrm{d}p_j}{2\pi\hbar}\right\}\\ \times \mathrm{e}^{-\frac{i}{\hbar}\sum_{j=1}^{N}p_j(x_{j+1}-x_j)}\left(\hat{A}\right)_{\mathrm{W}}[y_1,p_1]\\ \times \mathrm{e}^{-\frac{\beta}{N}\sum_{j=1}^{N}H(y_j,p_j)}\left(\mathrm{e}^{\frac{i\hat{H}t}{\hbar}}\hat{B}\,\mathrm{e}^{-\frac{i\hat{H}t}{\hbar}}\right)_{\mathrm{W}}[y_N,p_N],\end{aligned} \tag{9}$$

where $y_j = \frac{x_j+x_{j+1}}{2}$, $y_N = \frac{x_N+x_1}{2}$, and $H(y_j,p_j)$ is the classical Hamiltonian. Now, assuming that the potential energy $V(y_j)$ is independent of momentum, whereby most of the momenta only occur in the kinetic energy term of the classical Hamiltonians, $\frac{p_j^2}{2m}$, and the symplectic area, $\sum_{j=1}^{N}p_j(x_{j+1}-x_j)$, it is easy to integrate those momenta out analytically. The momenta that occur in other places in Eq. (9) are p_1 and p_N. p_1 can occur within the Wigner transform of $\hat{A}$. Depending on how $\left(\hat{A}\right)_{\mathrm{W}}[y_1,p_1]$ depends on p_1, the integration over p_1 will turn out differently. As long as $\int_{-\infty}^{\infty}\mathrm{d}p_1\left(\hat{A}\right)_{\mathrm{W}}[y_1,p_1]\,\mathrm{e}^{-\frac{\beta}{N}H(y_1,p_1)}\,\mathrm{e}^{-\frac{i}{\hbar}p_1(x_2-x_1)}$ can be evaluated analytically, e.g., for $\left(\hat{A}\right)_{\mathrm{W}}[y_1,p_1]$ being any polynomial of p_1 (see Appendix A), all momenta except p_N can be integrated out analytically. p_N can usually not be integrated out analytically since if $\hat{B}$ includes either position or momentum, then $\left(\mathrm{e}^{\frac{i\hat{H}t}{\hbar}}\hat{B}\,\mathrm{e}^{-\frac{i\hat{H}t}{\hbar}}\right)_{\mathrm{W}}[y_N,p_N]$ will depend on both, unless the potential is constant, and typically this dependence will be such that the integral is not easily evaluated analytically. Hence, these integrations lead to

$$\begin{aligned}\left\langle \hat{A}\hat{B}(t)\right\rangle = \lim_{N\to\infty}\frac{1}{Z}\left(\frac{mN}{2\pi\beta}\right)^{\frac{N}{2}}\sqrt{\frac{\beta}{2\pi mN}}\hbar^{-N}\left\{\prod_{j=1}^{N}\int_{-\infty}^{\infty}\mathrm{d}x_j\right\}\\ \times\int_{-\infty}^{\infty}\mathrm{d}p_N\,\mathrm{e}^{-\frac{i}{\hbar}p_N(x_1-x_N)}A'(y_1,x_2-x_1)\\ \times\mathrm{e}^{-\frac{mN}{2\hbar^2\beta}\sum_{j=1}^{N-1}(x_{j+1}-x_j)^2}\,\mathrm{e}^{-\frac{\beta}{N}\sum_{j=1}^{N}V(y_j)}\\ \times\mathrm{e}^{-\frac{\beta}{N}\frac{p_N^2}{2m}}\left(\mathrm{e}^{\frac{i\hat{H}t}{\hbar}}\hat{B}\,\mathrm{e}^{-\frac{i\hat{H}t}{\hbar}}\right)_{\mathrm{W}}[y_N,p_N],\end{aligned} \tag{10}$$

where $A'(y_1,x_2-x_1)$ is

$$\begin{aligned}A'(y_1,x_2-x_1) &= \frac{\int_{-\infty}^{\infty}\mathrm{d}p_1\left(\hat{A}\right)_{\mathrm{W}}[y_1,p_1]\,\mathrm{e}^{-\frac{\beta}{N}\frac{p_1^2}{2m}}\,\mathrm{e}^{-\frac{i}{\hbar}p_1(x_2-x_1)}}{\int_{-\infty}^{\infty}\mathrm{d}p_1\,\mathrm{e}^{-\frac{\beta}{N}\frac{p_1^2}{2m}}\,\mathrm{e}^{-\frac{i}{\hbar}p_1(x_2-x_1)}}\\ &= \frac{\int_{-\infty}^{\infty}\mathrm{d}p_1\left(\hat{A}\right)_{\mathrm{W}}[y_1,p_1]\,\mathrm{e}^{-\frac{\beta}{N}\frac{p_1^2}{2m}}\,\mathrm{e}^{-\frac{i}{\hbar}p_1(x_2-x_1)}}{\sqrt{\frac{2\pi mN}{\beta}}\,\mathrm{e}^{-\frac{\beta}{N}\frac{mN^2(x_2-x_1)^2}{2\hbar^2\beta^2}}}\end{aligned} \tag{11}$$

and may depend on y_1 and/or x_2-x_1.

Finally, the Wigner transform of the time-evolved operator $\hat{B}$ can be very difficult to derive. This is where the classical Wigner method comes in through the approximation $\left(\mathrm{e}^{\frac{i\hat{H}t}{\hbar}}\hat{B}\,\mathrm{e}^{-\frac{i\hat{H}t}{\hbar}}\right)_{\mathrm{W}}[y_N,p_N] \approx \left(\hat{B}\right)_{\mathrm{W}}[x(y_N,p_N,t),p(y_N,p_N,t)]$ [as in Eq. (3)] giving the final expression,

$$\begin{aligned}\left\langle \hat{A}\hat{B}(t)\right\rangle \approx \frac{1}{Z}\left(\frac{mN}{2\pi\beta}\right)^{\frac{N}{2}}\sqrt{\frac{\beta}{2\pi mN}}\hbar^{-N}\left\{\prod_{j=1}^{N}\int_{-\infty}^{\infty}\mathrm{d}x_j\right\}\\ \times\int_{-\infty}^{\infty}\mathrm{d}p_N\,\mathrm{e}^{-\frac{i}{\hbar}p_N(x_1-x_N)}\\ \times\mathrm{e}^{-\frac{\beta}{N}\left(\frac{p_N^2}{2m}+\sum_{j=1}^{N}V(y_j)+\frac{mN^2}{2\hbar^2\beta^2}\sum_{j=1}^{N-1}(x_{j+1}-x_j)^2\right)}\\ \times A'(y_1,x_2-x_1)\left(\hat{B}\right)_{\mathrm{W}}[x(y_N,p_N,t),p(y_N,p_N,t)],\end{aligned} \tag{12}$$

where $x(y_N,p_N,t)$ and $p(y_N,p_N,t)$ are the position and momentum coordinates describing the classical trajectory starting with y_N and p_N, and where also for practical reasons the limit of $N\to\infty$ has been removed, thereby also making the value of the correlation function at $t=0$ approximate. When referring to this expression, it will be called $\left\langle \hat{A}\hat{B}(t)\right\rangle_{y_1}$. It is noted that Eq. (12) is closely related to an expression recently published by Bose and Makri[12] [Eq. (2.7) in the reference], but not further explored by them. The main difference is that they use a Boltzmann operator that is symmetrized around $\hat{A}$, i.e., $\mathrm{e}^{-\frac{\beta}{2}\hat{H}}\hat{A}\,\mathrm{e}^{-\frac{\beta}{2}\hat{H}}$. Equation (12) is also related to the $L=1$ version of the method published by Bonella *et al.*,[13] more clearly seen in the paper by Bonella and Ciccotti.[14] This method also handles symmetrized Boltzmann operators but uses sum and difference variables for the polymer.

Apart from the asymmetric placement of the Boltzmann operator explored in this paper and the symmetric placement explored in the cited papers, another common handling of the Boltzmann operator is the Kubo transform.[24] This will not be further explored here; however, the Kubo transform of the new method can be found in Appendix B.

It can be noted that in Eq. (12), the effective equilibrium Hamiltonian has terms $\frac{mN^2}{2\hbar^2\beta^2}(x_{j+1}-x_j)^2$. These look exactly like the potential energy of harmonic springs and are, therefore, called "spring terms." This kind of model for a system is usually described as beads on a necklace, with the beads placed at the positions of the x_j:s and connected by springs. The ends of this polymer are connected via the imaginary exponential $-\frac{i}{\hbar}p_N(x_1-x_N)$, thus making it "open" in the sense that there is no force keeping the ends together, in contrast to other path integral methods such as path integral molecular dynamics,[25] ring polymer molecular dynamics,[3] or path integral Monte Carlo.[26] Even such a method as the open chain imaginary time path integral of Cendagorta *et al.*[27] would be considered a closed polymer from this point of view. A graphical representation of the open polymer in this work is shown in Fig. 1. This is the polymer advertised in the title of this paper.

Looking back at Eq. (7), it can be seen that if $\hat{A}$ only depends on the position, then $\hat{A}$ can operate to the left and transform into a function of x_1, $A(x_1)$, thereby leaving a matrix element of the Boltzmann operator. This operation removes the approximation of separating the Wigner transforms of $\hat{A}$ and $\mathrm{e}^{-\frac{\beta}{N}\hat{H}}$, making this derivation less approximate than the previous one. This means that a new version

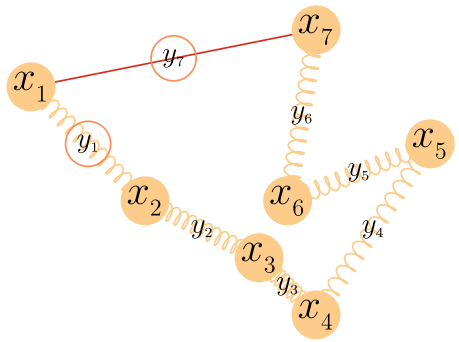

FIG. 1. A drawing to exemplify a 7-bead open polymer, where the positions of all the x:s and y:s have been marked. The springs represent the separations that give a spring-term, and the line is the separation that gives the imaginary exponential. y_1 and y_7 (in the circles) are where $A'(y_1, x_2 - x_1)$ and $\left(\hat{B}\right)_{\mathrm{W}}[x(y_7,p_7,t),p(y_7,p_7,t)]$ are evaluated, respectively.

of Eq. (12) is

$$\left\langle \hat{A}\hat{B}(t)\right\rangle \approx \frac{1}{Z}\left(\frac{mN}{2\pi\beta}\right)^{\frac{N}{2}}\sqrt{\frac{\beta}{2\pi mN}}\hbar^{-N}\left\{\prod_{j=1}^{N}\int_{-\infty}^{\infty}\mathrm{d}x_j\right\} \times \int_{-\infty}^{\infty}\mathrm{d}p_N\ \mathrm{e}^{-\frac{i}{\hbar}p_N(x_1-x_N)} \times \mathrm{e}^{-\frac{\beta}{N}\left(\frac{p_N^2}{2m}+\sum_{j=1}^{N}V(y_j)+\frac{mN^2}{2\hbar^2\beta^2}\sum_{j=1}^{N-1}(x_{j+1}-x_j)^2\right)} \times A(x_1)\left(\hat{B}\right)_{\mathrm{W}}[x(y_N,p_N,t),p(y_N,p_N,t)], \tag{13}$$

where the only change compared to before is that $A'(y_1, x_2 - x_1)$ has been replaced by $A(x_1)$. This expression will be referred to as $\left\langle \hat{A}\hat{B}(t)\right\rangle_{x_1}$. If $\hat{A}$ depends on both position and momentum, it is in many cases possible to reorder operators so that all position dependence is to the left of all momentum dependence, and then let the position dependent parts operate to the left in Eq. (7), keeping the momentum dependent parts in the matrix element. Of course this would lead to a more complicated expression than $A(x_1)$. Operators of both position and momentum will, however, not be further discussed in this article

If $\hat{A}$ depends only on momentum, then Eq. (12) will be equivalent to Eq. (13) so that $\left\langle \hat{A}\hat{B}(t)\right\rangle_{x_1} = \left\langle \hat{A}\hat{B}(t)\right\rangle_{y_1}$. For this situation, the notation $\left\langle \hat{A}\hat{B}(t)\right\rangle_{y_1,x_1}$ will be used.

For simplicity of notation, the path integral open polymer method will usually be called Open Polymer Classical Wigner, or OPCW for short, in this paper.

For multidimensional systems, the path integral open polymer method for sampling initial conditions can potentially get a severe sign problem due to the factor $\mathrm{e}^{-\frac{i}{\hbar}p_N(x_1-x_N)}$ appearing in each degree of freedom. The way this problem will be tackled in this article is to sample the initial distribution of the most quantum mechanical or most important degrees of freedom by the path integral open polymer method and the other degrees of freedom by classical mechanics, coupling each bead in the quantum mechanical part(s) with the single bead in the classical parts.

IV. COMPUTATIONAL DETAILS

Equations (12) and (13) were evaluated by Monte Carlo for the integrals over x_j and p_N and with molecular dynamics for the time propagation of $\left(\hat{B}\right)_{\mathrm{W}}[x(y_N,p_N,t),p(y_N,p_N,t)]$.

The correlation functions studied in this paper are autocorrelation functions of position, position-squared, momentum, and momentum-squared for a one-dimensional quartic potential. In addition, a one-dimensional double well potential and a quartic potential with many-dimensional harmonic baths were studied for the position and position-squared autocorrelation functions.

A. Potentials and system parameters

The potentials studied in this work are a quartic potential, a double well potential, and a quartic potential with various harmonic baths.

The quartic potential was taken as

$$V_{\mathrm{quartic}}(x) = \frac{m^2\omega^3}{4\hbar}x^4, \tag{14}$$

where ω is a unit of angular frequency.

The double well potential was taken as

$$V_{\mathrm{double\ well}}(x) = \frac{m^2\omega^3}{10\hbar}x^4 - \frac{1}{2}m\omega^2x^2. \tag{15}$$

The multidimensional systems all use the quartic potential together with the types of baths of Caldeira and Leggett.[28] These systems, thus, have one mostly quartic degree of freedom and several harmonic degrees of freedom that form a bath. The harmonic degrees of freedom in the bath are bilinearly coupled to the quartic degree of freedom. The form of the bath is the one suggested by Craig and Manolopoulos.[29] The bath is a discretized version of a bath with a linear spectral density with an exponential cutoff, and the parameters chosen for the current work are a cutoff frequency of ω and a system–bath coupling strength of $m\omega$. The complete potential is

$$V_{\mathrm{FD}}(x_1,x_2,\ldots,x_{F-1},x_F) = \frac{m^2\omega^3}{4\hbar}x_1^4 + \sum_{l=2}^{F}\frac{1}{2}m\omega^2\left(x_l\ln\left(\frac{l-\frac{3}{2}}{F-1}\right)+x_1\sqrt{\frac{2}{(F-1)\pi}}\right)^2, \tag{16}$$

where F is the number of degrees of freedom.

B. Monte Carlo

The maximum stepsize, $\Delta x_{\mathrm{max},l}$, was individually set for all degrees of freedom l, with an initial value of

$$\Delta x_{\mathrm{max},l} = \sqrt{\frac{2\ln 2}{F\beta\left(\left|\frac{\partial^2 V}{\partial x_l^2}\right|_{x_l=0}+\frac{m_l(N-1)N}{\hbar^2\beta^2}\right)}}. \tag{17}$$

This choice for stepsize is based on a harmonic approximation of the potential energy, assuming the same average stepsize in x_j and y_j, and aiming for 50% acceptance rate. The change in energy that would give an acceptance likelihood of 50% for a Monte Carlo step

is $N \ln 2/\beta$. $1/F$ of this energy could then be assigned to each degree of freedom. For each degree of freedom, the maximum stepsize is set so that the total energy change resulting from a change in position of $\Delta x_{\max,l}$ away from the minimum in the harmonically approximated potential, weighted by N, and the path integral spring potential, weighted by $N-1$, would give this energy. This results in Eq. (17). The above does not work for a situation where $\left|\frac{\partial^2 V}{\partial x_l^2}\right|_{x_l=0} = 0$ and at the same time $N = 1$, and in such cases, the maximum stepsize was set to the thermal de Broglie wavelength.

The maximal stepsizes were updated as a group every 50 000th step according to the algorithm of Allen and Tildesley[30] in order to keep the acceptance rate close to 50%.

The momentum, p_N, was sampled from a Maxwell–Boltzmann distribution at the temperature $\frac{N}{k_B\beta}$, where k_B is Boltzmann's constant. The pseudo-random number generator used was ran2 of Press *et al.*[31] Data were collected, i.e., a molecular dynamics trajectory was run, each 100th Monte Carlo-step.

The Monte Carlo chain begun in a part of phase space that has a low probability of occurring, i.e., far from the equilibrium distribution. It was, however, found that the number of Monte Carlo steps it takes to come close to equilibrium for the various simulated systems is negligible compared to the total length of the Monte Carlo simulation runs and was, therefore, not explicitly accounted for.

C. Molecular dynamics

The molecular dynamics was conducted using the velocity Verlet algorithm.[32,33] The time step was 0.050 ω^{-1} for the quartic and double well one-dimensional systems, and $0.035\omega^{-1}$, $0.025\omega^{-1}$, and $0.020\omega^{-1}$ for the quartic potential with harmonic baths containing 3, 6, and 9 degrees of freedom, respectively. The total time length of each molecular dynamics run was $10\omega^{-1}$.

D. Statistical evaluation of data

The block average method, explained by, e.g., Friedberg and Cameron[34] and Flegal, Haran, and Jones,[35] was used to calculate the standard deviations of the correlation functions. The minimum block size used was 10^6 Monte Carlo-steps. These standard deviations were used as a measure of uncertainty and to determine convergence.

E. Exact correlation functions

In order to have exact classical, quantum mechanical, and classical Wigner results to compare against, numerically exact results were produced for the systems and correlation functions where this was deemed doable.

For the quartic potential and double well potential, the classical mechanics comparison was obtained by setting N = 1, in the same program as was used to find the classical Wigner results, using 10^9 Monte Carlo steps.

The quantum mechanical autocorrelation functions for the quartic potential were calculated with a numerically exact program that uses the lowest 2000 particle in-the-box energy eigenfunctions, with a box length of $40\sqrt{\frac{\hbar}{m\omega}}$, as a basis set to approximate the 40 lowest energy eigenfunctions of the quartic oscillator. These eigenfunctions were then used to evaluate the necessary matrix elements and could be propagated in time analytically. The quantum mechanical autocorrelation functions for the double well potential were calculated in a similar way, but the basis set was the 12 lowest energy eigenfunctions of the harmonic oscillator, $V(x) = \frac{1}{2}m\omega^2x^2$.

For the quartic potential with harmonic bath, just as without the bath, a classical comparison was calculated with one bead, N = 1, in the classical Wigner routine, using 10^9 Monte Carlo steps. The quantum mechanical comparison at $t = 0$ for this case was a path integral Monte Carlo simulation with 80 beads, N = 80, run with the same Monte Carlo parameters as the classical Wigner runs. 64×10^9 Monte Carlo steps were used for 3 degrees of freedom in the bath and 16×10^9 Monte Carlo steps for 6 and 9 degrees of freedom in the bath.

The exact classical Wigner data were generated as follows: First, the matrix elements of the Boltzmann operator were calculated using the numerical matrix multiplication scheme.[36] In this scheme, $N = 50$ and $N = 14$ matrix multiplications of $e^{-\frac{\beta}{N}\hat{H}}$ were used for $\beta\hbar\omega = 8$ and $\beta\hbar\omega = 1$, respectively. Afterward, a numerical Fourier transform of these data was used for computing the Boltzmann Wigner transform. Finally, this Boltzmann Wigner function was represented on a grid for doing classical dynamics.

F. Feynman–Kleinert classical Wigner method

Many of the methods for acquiring an approximate initial distribution for a classical Wigner calculation use a harmonic approximation for the potential.[19,37,38] However, for potentials with negative curvature, these methods all encounter problems when the temperature is too low. For these situations, a modified local Gaussian approximation[39] can be used instead. This is, however, not necessary for the systems and temperatures in this paper.

The Feynman–Kleinert approximation[40] is one of the harmonic approximation methods, and its application to the classical Wigner method is usually called Feynman–Kleinert linearized path integral (FK-LPI).[37] FK-LPI will be used as a comparison for OPCW.

G. Ring polymer molecular dynamics

Ring polymer molecular dynamics (RPMD)[3] is a popular method for calculating approximate quantum dynamics. This method was used as a comparison for the classical Wigner results. The RPMD results were generated by using 32 and 5 beads for $\beta\hbar\omega = 8$ and $\beta\hbar\omega = 1$, respectively, using a time step of $0.009\omega^{-1}$ for the quartic oscillator and a time step of $0.0125\omega^{-1}$ for the double well and quartic oscillator with harmonic baths. The Kubo-transformed results acquired from the calculations were transformed into the asymmetric placement of the Boltzmann operator through the method by Braams, Miller, and Manolopoulos.[41] The way to calculate momentum-correlation functions with RPMD is through time derivatives of position correlation functions.[29,42] This was considered too complicated for $\langle \hat{p}^2\hat{p}^2(t)\rangle$ so that this function has not been included.

V. RESULTS AND DISCUSSION

In this section, the results from the calculations of a few different autocorrelation functions for a few model systems are presented. Each correlation function is presented by three lines. The middle

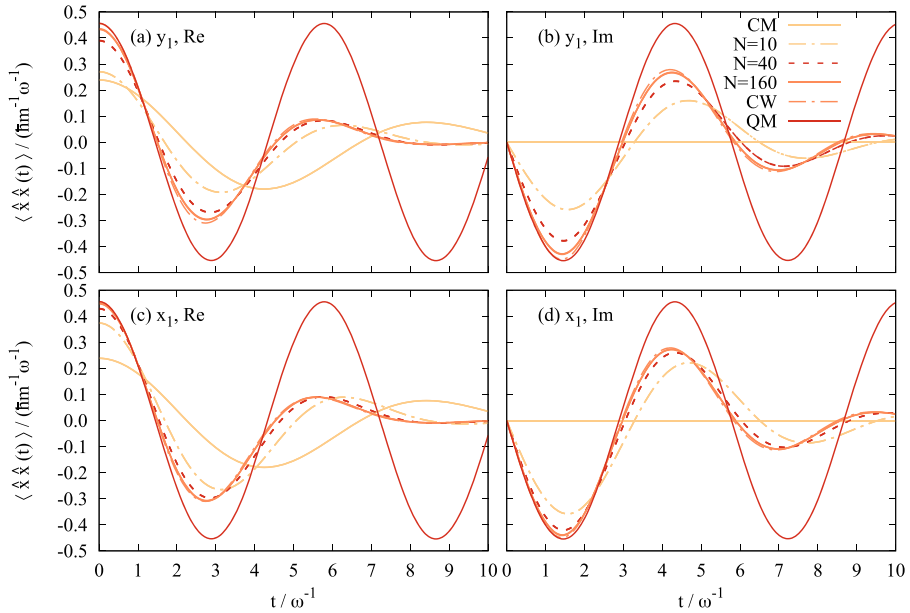

FIG. 2. The position autocorrelation function for a quartic potential ($\beta\hbar\omega$ = 8). Comparison between different numbers of beads for the two versions of OPCW and numerically exact solutions for classical mechanics (CM), classical Wigner (CW), and quantum mechanics (QM). The number of Monte Carlo steps used for each number of beads, N, is 1×10^9 for N = 10 and N = 40, and 16×10^9 for N = 160. The outer lines of each type show the standard deviations for the results. If the standard deviation is small enough, the outer lines are not visible. (a) Real part of $\langle \hat{x}\hat{x}(t) \rangle_{y_1}$, (b) imaginary part of $\langle \hat{x}\hat{x}(t) \rangle_{y_1}$, (c) real part of $\langle \hat{x}\hat{x}(t) \rangle_{x_1}$, and (d) imaginary part of $\langle \hat{x}\hat{x}(t) \rangle_{x_1}$.

line is the correlation function itself, and the upper and lower ones show the standard deviation of the result. In most cases presented here, the standard deviations are within the width of the middle line.

A. Quartic potential $\beta\hbar\omega$ = 8

When looking at the correlation functions for the quartic potential calculated with the new method (Figs. 2–4) and numerically exact classical Wigner (Figs. 2 and 3), it can be seen that they flatten out and become constant at long times. This is due to the fact that the classical Wigner method relies on classical mechanics for propagation forward in time. For all systems with potentials of higher order than harmonic, the classical trajectories do not give the correct coherence, meaning that the individual classical trajectories dephase against each other. Results for a one-dimensional harmonic oscillator, where classical propagation is exact, can be found in Appendix C. Analytic expressions for the harmonic oscillator autocorrelation functions have been placed in Appendix D.

In Fig. 2, it can be seen that at time t = 0, the correlation functions calculated with the new method converge from classical

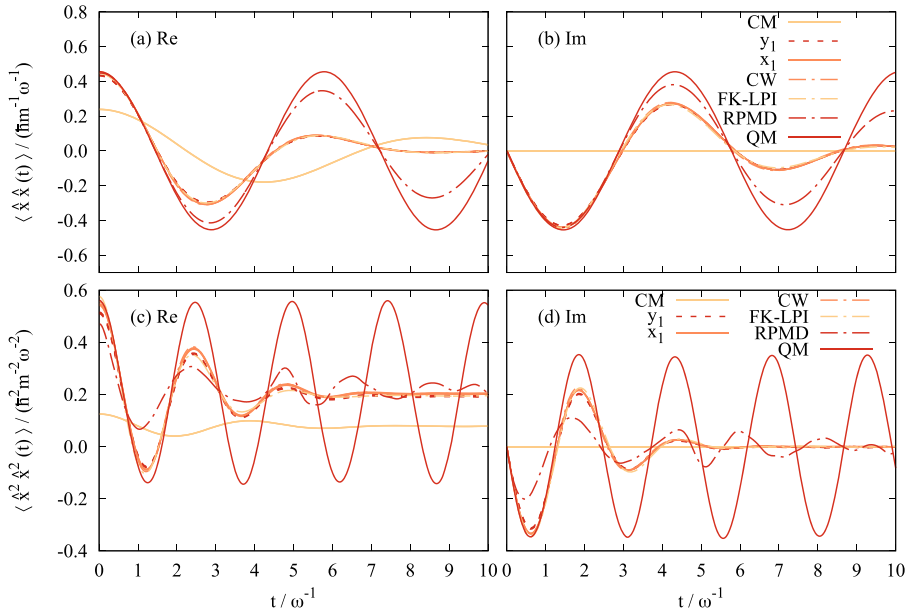

FIG. 3. The position and position-squared autocorrelation functions for a quartic potential ($\beta\hbar\omega$ = 8). Comparison between the two versions of OPCW and numerically exact solutions for classical mechanics (CM), classical Wigner (CW), FK-LPI, RPMD, and quantum mechanics (QM). The number of beads used in the y_1- and x_1-calculations is N = 160, and the number of Monte Carlo steps is 16×10^9. The outer lines of each type show the standard deviations for the results. If the standard deviation is small enough, the outer lines are not visible. (a) Real part of $\langle \hat{x}\hat{x}(t) \rangle$, (b) imaginary part of $\langle \hat{x}\hat{x}(t) \rangle$, (c) real part of $\langle \hat{x}^2\hat{x}^2(t) \rangle$, and (d) imaginary part of $\langle \hat{x}^2\hat{x}^2(t) \rangle$.

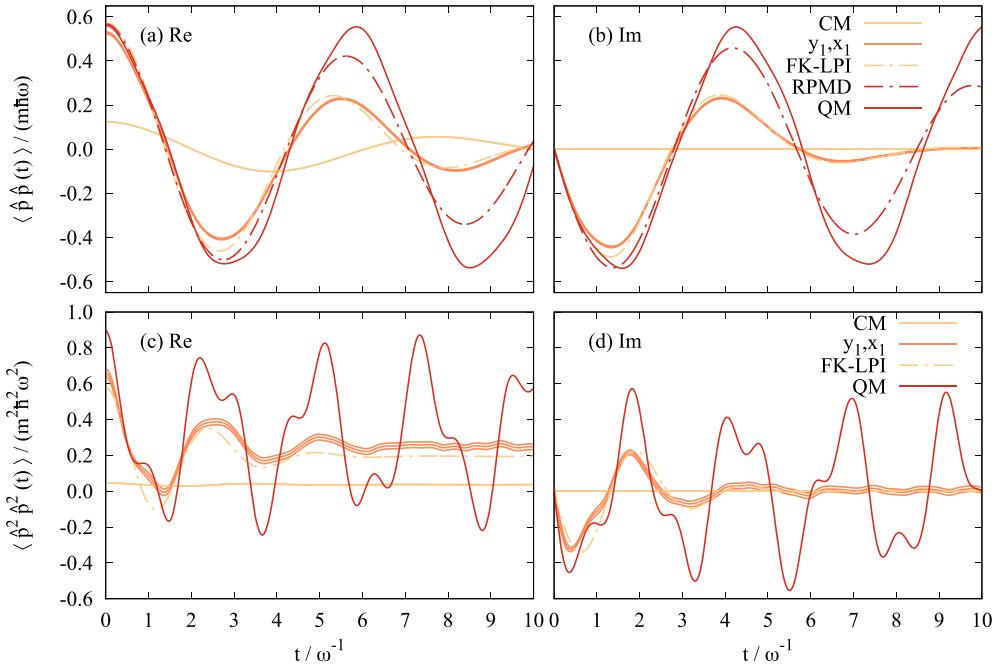

FIG. 4. The momentum and momentum-squared autocorrelation functions for a quartic potential ($\beta\hbar\omega = 8$). Comparison between OPCW [with $\langle\hat{p}\hat{p}(t)\rangle_{y_1}$ and $\langle\hat{p}^2\hat{p}^2(t)\rangle_{y_1}$ being identical to $\langle\hat{p}\hat{p}(t)\rangle_{x_1}$ and $\langle\hat{p}^2\hat{p}^2(t)\rangle_{x_1}$, respectively] and numerically exact solutions for classical mechanics (CM), FK-LPI, RPMD, and quantum mechanics (QM). The number of beads used in the calculations of $\langle\hat{p}\hat{p}(t)\rangle_{y_1,x_1}$ is $N = 160$, and the number of Monte Carlo steps is 64×10^9. The number of beads used in the calculations of $\langle\hat{p}^2\hat{p}^2(t)\rangle_{y_1,x_1}$ is $N = 80$, and the number of Monte Carlo steps is 128×10^9. The outer lines of each type show the standard deviations for the results. If the standard deviation is small enough, the outer lines are not visible. (a) Real part of $\langle\hat{p}\hat{p}(t)\rangle$, (b) imaginary part of $\langle\hat{p}\hat{p}(t)\rangle$, (c) real part of $\langle\hat{p}^2\hat{p}^2(t)\rangle$, and (d) imaginary part of $\langle\hat{p}^2\hat{p}^2(t)\rangle$.

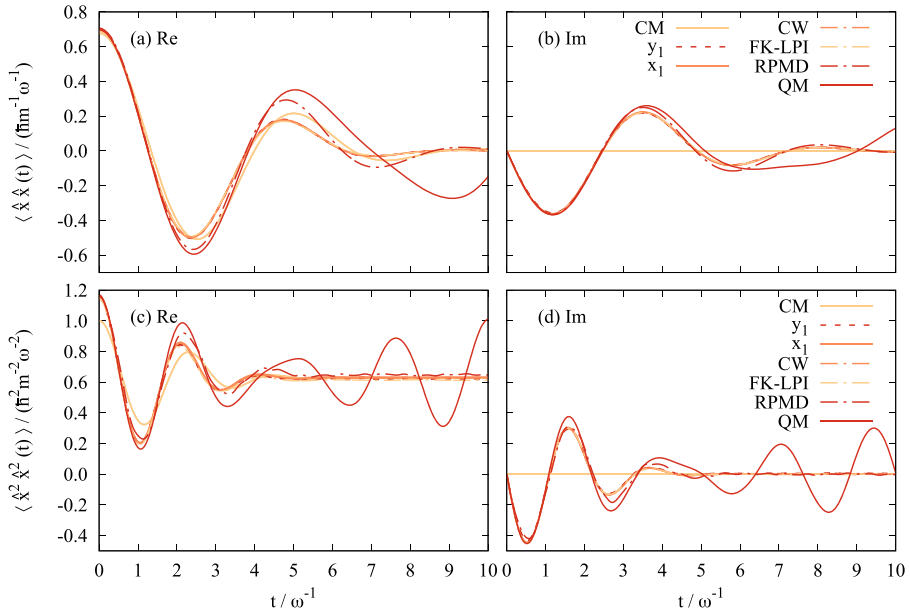

FIG. 5. The position and position-squared autocorrelation functions for a quartic potential ($\beta\hbar\omega = 1$). Comparison between the two versions of OPCW and numerically exact solutions for classical mechanics (CM), classical Wigner (CW), FK-LPI, RPMD, and quantum mechanics (QM). The number of beads used in the y_1- and x_1-calculations of $\langle\hat{x}\hat{x}(t)\rangle$ is $N = 80$, and the number of Monte Carlo steps is 16×10^9. The number of beads used in the y_1- and x_1-calculations of $\langle\hat{x}^2\hat{x}^2(t)\rangle$ is $N = 80$, and the number of Monte Carlo steps is 64×10^9. The outer lines of each type show the standard deviations for the results. If the standard deviation is small enough, the outer lines are not visible. (a) Real part of $\langle\hat{x}\hat{x}(t)\rangle$, (b) imaginary part of $\langle\hat{x}\hat{x}(t)\rangle$, (c) real part of $\langle\hat{x}^2\hat{x}^2(t)\rangle$, and (d) imaginary part of $\langle\hat{x}^2\hat{x}^2(t)\rangle$.

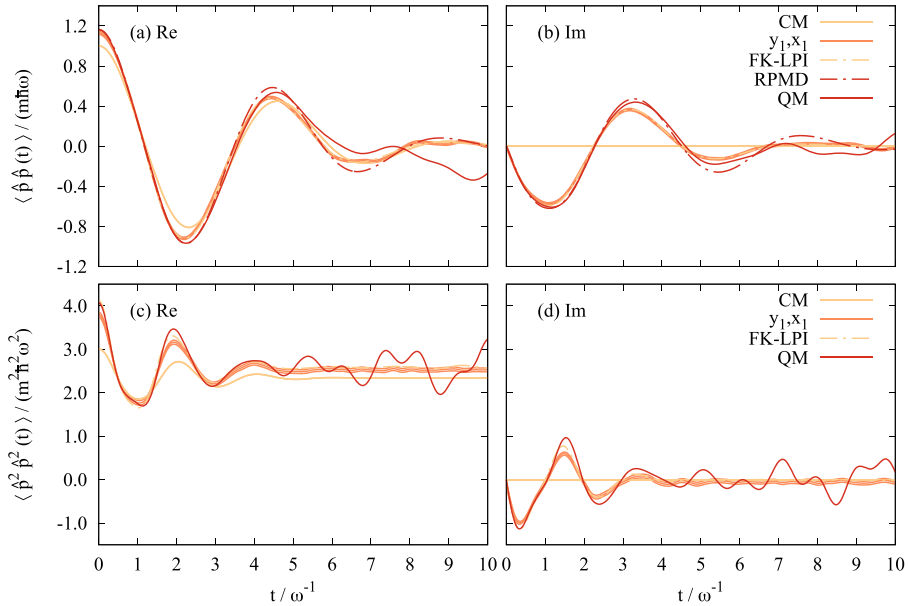

FIG. 6. The momentum and momentum-squared autocorrelation functions for a quartic potential ($\beta\hbar\omega$ = 1). Comparison between OPCW [with $\langle\hat{p}\hat{p}(t)\rangle_{y_1}$ and $\langle\hat{p}^2\hat{p}^2(t)\rangle_{y_1}$ being identical to $\langle\hat{p}\hat{p}(t)\rangle_{x_1}$ and $\langle\hat{p}^2\hat{p}^2(t)\rangle_{x_1}$, respectively] and numerically exact solutions for classical mechanics (CM), FK-LPI, RPMD, and quantum mechanics (QM). The number of beads used in the calculations of $\langle\hat{p}\hat{p}(t)\rangle_{y_1,x_1}$ is N = 80, and the number of Monte Carlo steps is 128 × 10^9. The number of beads used in the calculations of $\langle\hat{p}^2\hat{p}^2(t)\rangle_{y_1,x_1}$ is N = 20, and the number of Monte Carlo steps is 256 × 10^9. The outer lines of each type show the standard deviations for the results. If the standard deviation is small enough, the outer lines are not visible. (a) Real part of $\langle\hat{p}\hat{p}(t)\rangle_{y_1,x_1}$, (b) imaginary part of $\langle\hat{p}\hat{p}(t)\rangle_{y_1,x_1}$, (c) real part of $\langle\hat{p}^2\hat{p}^2(t)\rangle_{y_1,x_1}$, and (d) imaginary part of $\langle\hat{p}^2\hat{p}^2(t)\rangle_{y_1,x_1}$.

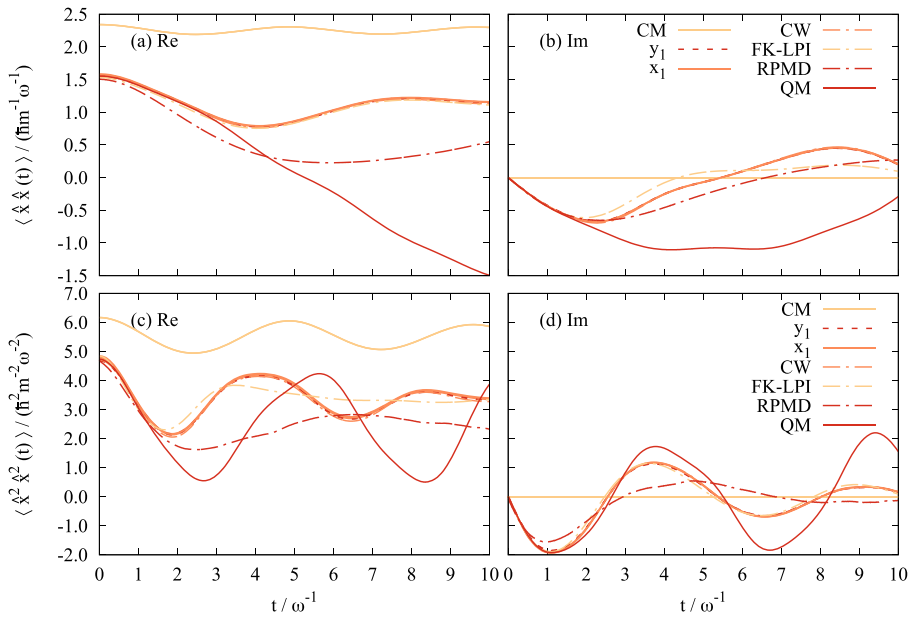

FIG. 7. The position and position-squared autocorrelation functions for a double well potential ($\beta\hbar\omega$ = 8). Comparison between the two versions of OPCW and numerically exact solutions for classical mechanics (CM), classical Wigner (CW), FK-LPI, RPMD, and quantum mechanics (QM). The number of beads used in the y_1- and x_1-calculations is N = 160, and the number of Monte Carlo steps is 16 × 10^9. The outer lines of each type show the standard deviations for the results. If the standard deviation is small enough, the outer lines are not visible. (a) Real part of $\langle\hat{x}\hat{x}(t)\rangle$, (b) imaginary part of $\langle\hat{x}\hat{x}(t)\rangle$, (c) real part of $\langle\hat{x}^2\hat{x}^2(t)\rangle$, and (d) imaginary part of $\langle\hat{x}^2\hat{x}^2(t)\rangle$.

mechanics toward quantum mechanics as the number of beads is increased. For all times, the correlation functions calculated with the new method converge toward the exact classical Wigner method. It can also be seen that the x_1-method converges faster than the y_1-method with respect to the number of beads. This is also the case for the harmonic oscillator, see Appendix E, where an explanation for this is also given.

Looking at the individual versions of the new method in Figs. 2 and 3, it can be seen that at least the real parts of $\langle \hat{x}\hat{x}(t)\rangle_{x_1}$ and $\langle \hat{x}^2\hat{x}^2(t)\rangle_{x_1}$ have converged essentially to within the thickness of the line of the exact classical Wigner result for $N = 160$. $\langle \hat{x}\hat{x}(t)\rangle_{y_1}$ and $\langle \hat{x}^2\hat{x}^2(t)\rangle_{y_1}$ converge quite slowly in comparison, and the results for $N = 160$ are not entirely converged to the exact classical Wigner result, even if they are close. $\langle \hat{p}\hat{p}(t)\rangle_{y_1,x_1}$ in Figs. 4(a) and 4(b) has not converged all the way to exact quantum mechanics at $t = 0$ for $N = 160$ but is close.

In Figs. 4(c) and 4(d), it stands out that $\langle \hat{p}^2\hat{p}^2(t)\rangle_{y_1,x_1}$ is far from converged to exact quantum mechanics at $t = 0$, but this is a complicated correlation function. Even though the result for $N = 80$ is not very close to exact quantum mechanics at time $t = 0$, the shapes of the curves have some qualitative agreement.

Correlation functions with $\hat{p}^n$ in the first operator can be expected to be more difficult to converge than correlation functions with $\hat{x}^n$ in the first operator, since $(\hat{p}^n)_W$ will be integrated into an nth-order polynomial of a difference between positions, while $(\hat{x}^n)_W$ will just be a position, or an average of positions, to the power of n (see Appendix A).

In Fig. 3, it can be seen that FK-LPI gives results very close to exact classical Wigner for $\langle \hat{x}\hat{x}(t)\rangle$ and the imaginary part of $\langle \hat{x}^2\hat{x}^2(t)\rangle$, while the real part of $\langle \hat{x}^2\hat{x}^2(t)\rangle$ is a little bit further off. OPCW gives as good, or slightly better, results as FK-LPI, except y_1 for $\mathrm{Im}\langle \hat{x}^2\hat{x}^2(t)\rangle$.

In Figs. 4(a) and 4(b), it can be seen that FK-LPI gives a better starting value for $\langle \hat{p}\hat{p}(t)\rangle$ than the calculations with the new method. The oscillations are, however, qualitatively similar. For $\langle \hat{p}^2\hat{p}^2(t)\rangle$ in Figs. 4(c) and 4(d), the results acquired with the new method have a better value at $t = 0$ and has more qualitative agreement with the exact quantum mechanical result than the FK-LPI result.

It is shown in Figs. 3, 4(a), and 4(b) that the classical Wigner method gives worse amplitudes than RPMD for the linear autocorrelation functions, $\langle \hat{x}\hat{x}(t)\rangle$ and $\langle \hat{p}\hat{p}(t)\rangle$. It can, however, also be seen that the classical Wigner method gives better amplitude at short times and better phase overall than RPMD does for the non-linear autocorrelation function $\langle \hat{x}^2\hat{x}^2(t)\rangle$. This is not surprising as it is known that for RPMD to be exact for the harmonic oscillator at least one of the operators in a correlation function has to be linear.[3]

B. Quartic potential $\beta\hbar\omega = 1$

When, for the quartic potential, the temperature is increased so that $\beta\hbar\omega = 1$, instead of $\beta\hbar\omega = 8$, it is shown in Fig. 5 that $\langle \hat{x}\hat{x}(t)\rangle$ and $\langle \hat{x}^2\hat{x}^2(t)\rangle$ for both versions of the new method are almost perfectly converged to the exact classical Wigner result for $N = 80$. This is fewer beads than what seems necessary to achieve a similar convergence at $\beta\hbar\omega = 8$. This is hardly surprising as the classical and quantum mechanical correlation functions are much more similar at $\beta\hbar\omega = 1$ than at $\beta\hbar\omega = 8$.

In Fig. 6, it can be seen that $\langle \hat{p}\hat{p}(t)\rangle_{y_1,x_1}$ is rather well converged toward exact quantum mechanics at $t = 0$. $\langle \hat{p}^2\hat{p}^2(t)\rangle_{y_1,x_1}$ does not reach the limit of the exact quantum mechanics for the $N = 20$ calculation presented here but shows a qualitative agreement with quantum mechanics up to $t = 4\omega^{-1}$

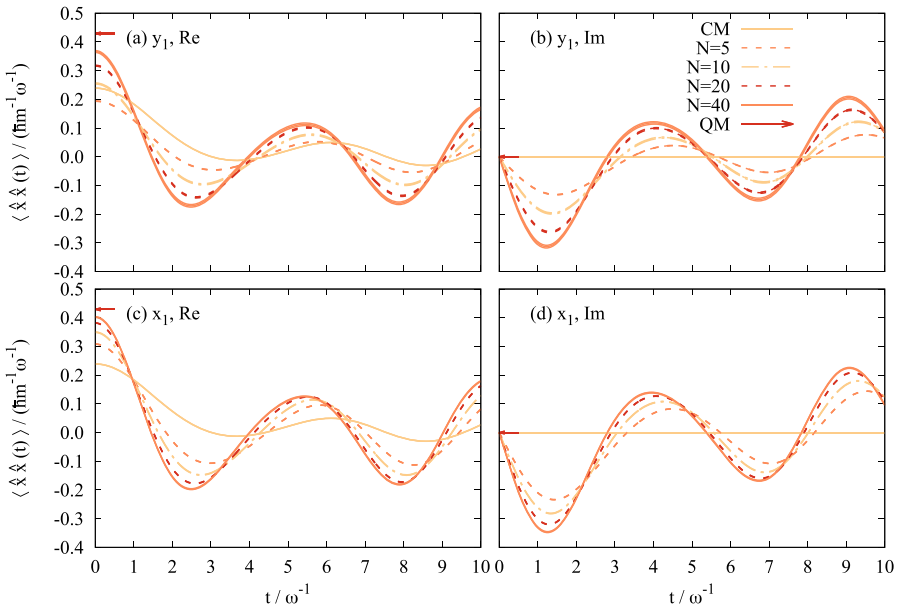

FIG. 8. The position autocorrelation function for a quartic potential with a harmonic bath with 3 degrees of freedom ($\beta\hbar\omega = 8$). Comparison between different numbers of beads for the two versions of OPCW and numerically exact solutions for classical mechanics (CM), at all times and quantum mechanics (QM), at time $t = 0$. The number of Monte Carlo steps used for each number of beads, N, is 1×10^9 for $N = 5$ and $N = 10$, 16×10^9 for $N = 20$, and 64×10^9 for $N = 40$. The outer lines of each type show the standard deviations for the results. If the standard deviation is small enough, the outer lines are not visible. (a) Real part of $\langle \hat{x}\hat{x}(t)\rangle_{y_1}$, (b) imaginary part of $\langle \hat{x}\hat{x}(t)\rangle_{y_1}$, (c) real part of $\langle \hat{x}\hat{x}(t)\rangle_{x_1}$, and (d) imaginary part of $\langle \hat{x}\hat{x}(t)\rangle_{x_1}$.

Generally, even for a lower number of beads the convergence with respect to the number of Monte Carlo steps is worse for $\beta\hbar\omega = 1$ compared to $\beta\hbar\omega = 8$. This is, however, not a problem in practice as fewer beads are required to converge the result to the exact classical Wigner result at the higher temperature.

For $\langle\hat{x}\hat{x}(t)\rangle$ and $\langle\hat{x}^2\hat{x}^2(t)\rangle$, FK-LPI results are essentially the same as the exact classical Wigner results. For $\langle\hat{p}\hat{p}(t)\rangle$, the results from the new method and the FK-LPI results are very similar. However, for $\langle\hat{p}^2\hat{p}^2(t)\rangle$, the FK-LPI results are somewhat closer to the quantum mechanical result than the results produced with OPCW.

For $\langle\hat{x}\hat{x}(t)\rangle$, the classical Wigner method gives worse amplitudes than RPMD. For $\langle\hat{x}^2\hat{x}^2(t)\rangle$, the classical Wigner method possibly gets a somewhat worse amplitude than RPMD. For $\langle\hat{p}\hat{p}(t)\rangle$, it is not obvious if one of the methods performs better than the other.

C. Double well potential $\beta\hbar\omega = 8$

In Fig. 7, it can be seen that all the approximate methods quite early become very different from exact quantum mechanics. This is because dynamical tunneling is important for describing the dynamics of a system like this, which is not taken into account at all in the classical Wigner method and not properly in RPMD. For $\langle\hat{x}\hat{x}(t)\rangle$, the y_1- and x_1-versions of the open polymer method have converged to the exact classical Wigner result by using 160 beads. For $\langle\hat{x}^2\hat{x}^2(t)\rangle$, the open polymer method has almost converged to the exact classical Wigner result using 160 beads.

The FK-LPI results can be seen to essentially agree with the exact classical Wigner result for the real part of $\langle\hat{x}\hat{x}(t)\rangle$ and to be close to it for the imaginary part of $\langle\hat{x}^2\hat{x}^2(t)\rangle$. For the other cases, FK-LPI is further off. For the real part of $\langle\hat{x}^2\hat{x}^2(t)\rangle$, FK-LPI is substantially off compared to exact classical Wigner. The FK-LPI results do, however, stay almost equal to the exact quantum mechanical results for as long as the exact classical Wigner results do.

The classical Wigner method gives significantly better results than RPMD for the real part of $\langle\hat{x}\hat{x}(t)\rangle$ and the imaginary part of $\langle\hat{x}^2\hat{x}^2(t)\rangle$, and slightly better results for the real part of $\langle\hat{x}^2\hat{x}^2(t)\rangle$. For the imaginary part of $\langle\hat{x}\hat{x}(t)\rangle$, the classical Wigner method and RPMD perform equally well.

D. Quartic potential in harmonic bath $\beta\hbar\omega = 8$

In Figs. 8 and 9, the position and position-squared autocorrelation functions are shown for the quartic oscillator with a harmonic bath of 3 degrees of freedom. The numerically exact quantum mechanical comparison is only available for time $t = 0$ due to the method used for its calculation (see Sec. IV E). It can, in these figures, be seen that the new method converges from classical mechanics toward quantum mechanics at $t = 0$ as the number of beads is increased. The possible exception is for low

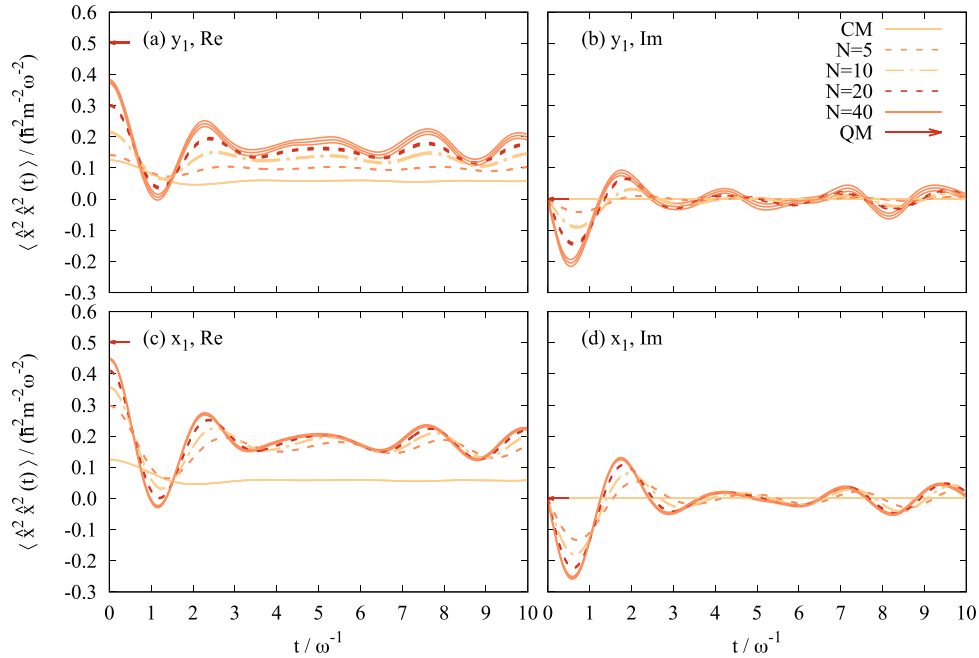

FIG. 9. The position-squared autocorrelation function for a quartic potential with a harmonic bath with 3 degrees of freedom ($\beta\hbar\omega = 8$). Comparison between different numbers of beads for the two versions of OPCW and numerically exact solutions for classical mechanics (CM), at all times and quantum mechanics (QM), at time $t = 0$. The number of Monte Carlo steps used for each number of beads, N, is 1×10^9 for $N = 5$ and $N = 10$, 16×10^9 for $N = 20$, and 64×10^9 for $N = 40$. The outer lines of each type show the standard deviations for the results. If the standard deviation is small enough, the outer lines are not visible. The value in parentheses gives the number of Monte Carlo steps. (a) Real part of $\langle\hat{x}^2\hat{x}^2(t)\rangle_{y_1}$, (b) imaginary part of $\langle\hat{x}^2\hat{x}^2(t)\rangle_{y_1}$, (c) real part of $\langle\hat{x}^2\hat{x}^2(t)\rangle_{x_1}$, and (d) imaginary part of $\langle\hat{x}^2\hat{x}^2(t)\rangle_{x_1}$.

numbers of beads for y_1, as for $N = 5$ $\mathrm{Re}\langle\hat{x}\hat{x}(t)\rangle_{y_1}$ is further from the quantum mechanical result than classical mechanics is.

In Figs. 10–12, the position and position-squared autocorrelation functions are shown for the quartic oscillator with a harmonic bath of 3, 6, and 9 degrees of freedom, respectively.

In Figs. 8, 9, 11, and 12, it can be seen that the x_1-results are significantly closer to quantum mechanics at $t = 0$ than the y_1-results are.

For the case with 3 degrees of freedom in the bath, results are shown that are not entirely converged with respect to the number of Monte Carlo steps used, and it is visible that the x_1-version of the method converges better with respect to the number of Monte Carlo steps than the y_1-version.

Overall, the calculations for the larger numbers of degrees of freedom are fairly computationally intensive and have, therefore, not been numerically converged with respect to the number of beads. However, it is shown in Figs. 10–12 that when the harmonic bath is sampled from a classical distribution, much larger numbers of beads can be used in the quartic oscillator degree of freedom and the number of Monte Carlo steps used is still the same or smaller than used for a one-dimensional quartic potential with a lower number of beads. Making the bath classical, thus, improves the overall convergence drastically. The classical bath calculations are so well converged with regard to both numbers of beads and Monte Carlo steps that the difference between y_1 and x_1 is almost unnoticeable for the correlation functions shown here, and therefore, only the x_1-version is shown. The difference in numerical performance between the full OPCW calculations and the calculations with classical bath can be seen to increase when the size of the bath is increased.

At time $t = 0$, the calculations employing a classical bath give better values than those using the open polymer for all degrees of freedom. However, even if the quartic oscillator part of a classical bath calculation were to be sampled with an infinite number of beads in the polymer, the classical mechanics of the bath would still mean that the initial value of the correlation functions would not necessarily be the exact quantum mechanical value. The correlation functions for $t > 0$ for the classical bath calculations are qualitatively similar to but have higher amplitudes than the full OPCW calculations. This is the behavior that would be expected from a full OPCW calculation with a larger number of beads.

For the real part of $\langle\hat{x}^2\hat{x}^2(t)\rangle$, the long time value given by the classical bath calculations is lower than the corresponding result for the full OPCW calculations, except y_1 for 9 degrees of freedom in the bath. From the full OPCW results for the quartic oscillator with a harmonic bath with 3 degrees of freedom (Figs. 8 and 9) and the one-dimensional quartic oscillator (Fig. 2), it can be expected that for the same number of beads in the open polymer, x_1 will be more converged toward exact classical Wigner than y_1 will be. For the quartic oscillator with harmonic baths with 6 and 9 degrees of freedom, Figs. 11 and 12, the results from calculations with classical baths are closer to the y_1-results than to the x_1-results. This indicates that the long time values of $\mathrm{Re}\langle\hat{x}^2\hat{x}^2(t)\rangle$ may not be very well described

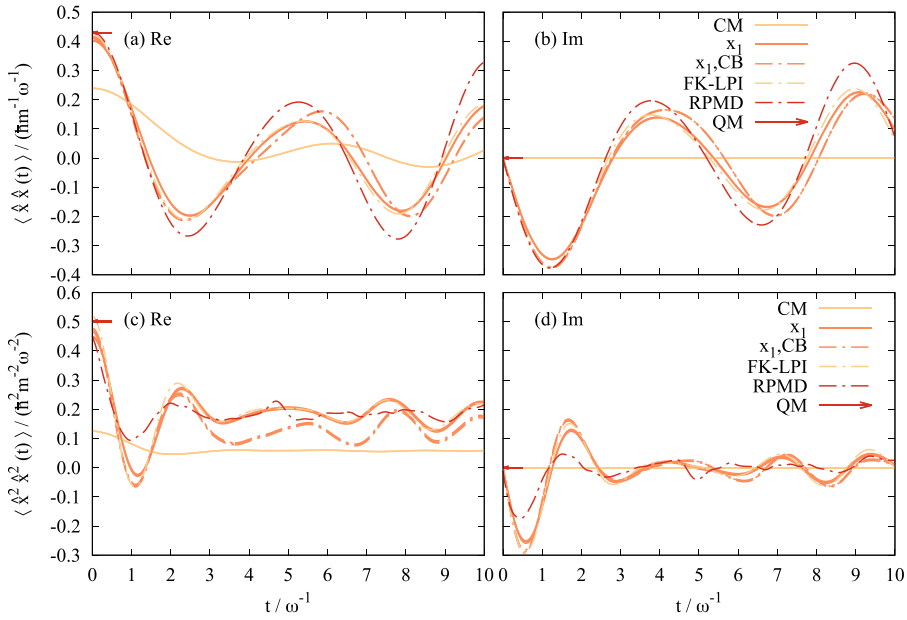

FIG. 10. The position and position-squared autocorrelation functions for a quartic potential with a harmonic bath with 3 degrees of freedom ($\beta\hbar\omega = 8$). Comparison between the x_1-version of OPCW and numerically exact solutions for classical mechanics (CM), FK-LPI, and RPMD, at all times and quantum mechanics (QM), at time $t = 0$. Results for the x_1-version of OPCW with 320 beads in the quartic oscillator and a classical bath, CB, are also shown. The number of beads used in the y_1- and x_1-calculations is $N = 40$, and the number of Monte Carlo steps is 64×10^9. For the calculations with classical bath, the number of Monte Carlo steps used is 16×10^9. The outer lines of each type show the standard deviations for the results. If the standard deviation is small enough, the outer lines are not visible. (a) Real part of $\langle\hat{x}\hat{x}(t)\rangle$, (b) imaginary part of $\langle\hat{x}\hat{x}(t)\rangle$, (c) real part of $\langle\hat{x}^2\hat{x}^2(t)\rangle$, and (d) imaginary part of $\langle\hat{x}^2\hat{x}^2(t)\rangle$.

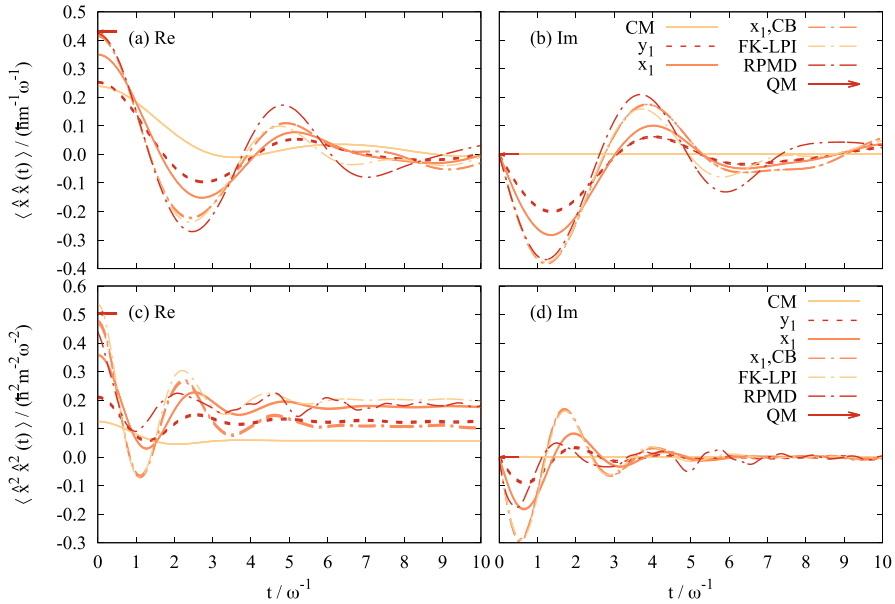

FIG. 11. The position and position-squared autocorrelation functions for a quartic potential with a harmonic bath with 6 degrees of freedom ($\beta\hbar\omega = 8$). Comparison between the two versions of OPCW and numerically exact solutions for classical mechanics (CM), FK-LPI, and RPMD, at all times and quantum mechanics (QM), at time $t = 0$. Results for the x_1-version of OPCW with 320 beads in the quartic oscillator and a classical bath, CB, are also shown. The number of beads used in the y_1- and x_1-calculations is $N = 10$, and the number of Monte Carlo steps is 64×10^9. For the calculations with classical bath, the number of Monte Carlo steps used is 16×10^9. The outer lines of each type show the standard deviations for the results. If the standard deviation is small enough, the outer lines are not visible. (a) Real part of $\langle \hat{x}\hat{x}(t) \rangle$, (b) imaginary part of $\langle \hat{x}\hat{x}(t) \rangle$, (c) real part of $\langle \hat{x}^2\hat{x}^2(t) \rangle$, and (d) imaginary part of $\langle \hat{x}^2\hat{x}^2(t) \rangle$.

with the classical bath. This was to be expected as the zero point energy leakage from the system into the bath should be considerable in this type of calculation, and the correlation function, even at long times, is highly dependent on the magnitude of the oscillation in the system degree of freedom.

It can be seen in Figs. 10–12 that the results from the classical bath calculations and the FK-LPI results follow each other closely for the first 2–4 ω^{-1}. At $t = 0$, the classical bath results are as good as or slightly worse than the FK-LPI results.

In Figs. 10(a), 10(b), 11(a), 11(b), 12(a), and 12(b), it can be seen that the classical Wigner method with a classical bath gives slightly worse than or equally good results as RPMD does for $\langle \hat{x}\hat{x}(t) \rangle$ at $t = 0$. Looking at Figs. 10(c), 10(d), 11(c), 11(d), 12(c), and 12(d), it can be seen that the classical Wigner method with a classical bath gives slightly better results than RPMD does for $\langle \hat{x}^2\hat{x}^2(t) \rangle$ at $t = 0$. RPMD, however, goes to higher values at long times for the real part of $\langle \hat{x}^2\hat{x}^2(t) \rangle$, and this may be a better value as it follows $\langle \hat{x}^2\hat{x}^2(t) \rangle_{x_1}$, which should be better converged than $\langle \hat{x}^2\hat{x}^2(t) \rangle_{y_1}$.

E. Summary of results

For all the cases studied here, the results of the new method converge toward exact quantum mechanics at time $t = 0$ as the number of beads increases. Additionally, for all cases where the exact classical Wigner result is available, the new method converges toward this result as the number of beads increases. These convergences are what should be observed according to the derivation of the method. Some of the results for the one-dimensional quartic oscillator and double well have converged essentially to within the thickness of the line of the exact classical Wigner result.

For the correlation functions where a comparison has been made, the x_1-version of the new method converges faster than the y_1-version with respect to the number of beads used. The x_1-version also converges better than the y_1-version with respect to the number of Monte Carlo steps for these cases. Note also that for almost every graph shown, it can be seen that for a larger number of beads, more Monte Carlo steps have been used to converge the results.

The results for the multidimensional systems using many beads in the polymer for sampling the initial distribution of the quartic oscillator degree of freedom and classical mechanics to sample the initial distribution of the bath show a significant improvement in convergence toward the exact result at $t = 0$ compared to the results of using fewer beads for the full OPCW quartic oscillator with harmonic bath. The long time values of $\mathrm{Re}\langle \hat{x}^2\hat{x}^2(t) \rangle$ may, however, be significantly different from the exact classical Wigner result. This is likely to be a result of increased zero point energy leakage when a classical bath is used.

If looking at the one-dimensional and multidimensional potentials, using a classical bath for the multidimensional cases, the results from the open polymer sampled classical Wigner method is about as good as the results from FK-LPI. For the double well potential, the new method clearly reproduces the exact classical Wigner results better than FK-LPI, but the new method does not come closer to

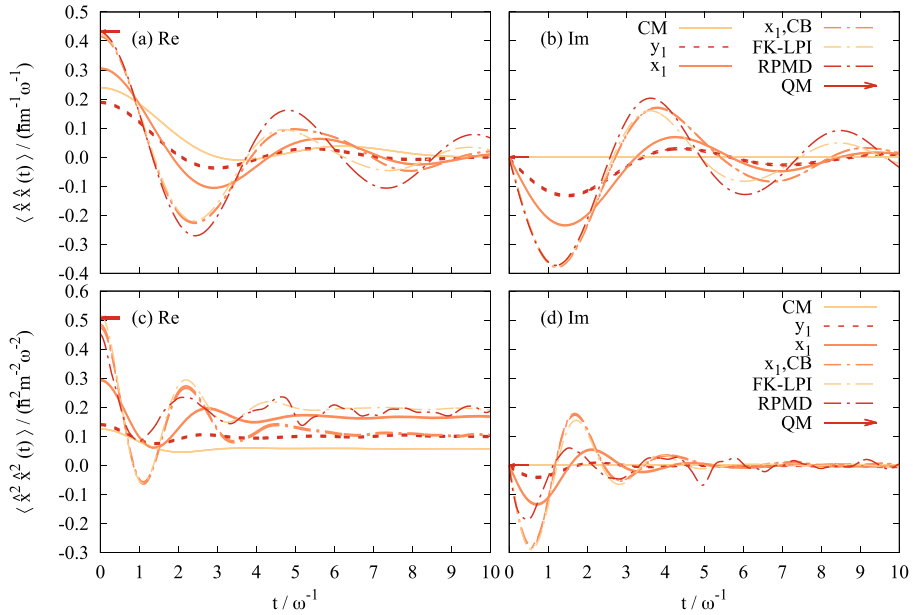

FIG. 12. The position and position-squared autocorrelation functions for a quartic potential with a harmonic bath with 9 degrees of freedom ($\beta\hbar\omega$ = 8). Comparison between the two versions of OPCW and numerically exact solutions for classical mechanics (CM), FK-LPI, and RPMD, at all times and quantum mechanics (QM), at time t = 0. Results for the x_1-version of OPCW with 320 beads in the quartic oscillator and a classical bath, CB, are also shown. The number of beads used in the y_1- and x_1-calculations is N = 5, and the number of Monte Carlo steps is 16×10^9. For the calculations with classical bath, the number of Monte Carlo steps used is 16×10^9. The outer lines of each type show the standard deviations for the results. If the standard deviation is small enough, the outer lines are not visible. (a) Real part of $\langle \hat{x}\hat{x}(t)\rangle$, (b) imaginary part of $\langle \hat{x}\hat{x}(t)\rangle$, (c) real part of $\langle \hat{x}^2\hat{x}^2(t)\rangle$, and (d) imaginary part of $\langle \hat{x}^2\hat{x}^2(t)\rangle$.

exact quantum mechanics than FK-LPI. Comparing Figs. 3, 5, and 7, it can be seen that the OPCW method works essentially equally well independent of the potential involved, while in the case of FK-LPI, it works worse for the double well, which contains a region of negative curvature.

In comparison to RPMD, it can be seen that for the one-dimensional quartic oscillator, the classical Wigner method and thereby also the OPCW method perform worse than, or in a single case equally well as, RPMD for autocorrelation functions of linear operators. For the autocorrelation function $\langle \hat{x}^2\hat{x}^2(t)\rangle$, the classical Wigner method gives better results than RPMD at the lower temperature employed here and possibly worse results at the higher temperature. For the one-dimensional double well potential, the classical Wigner method is seen to give better results than RPMD for both $\langle \hat{x}\hat{x}(t)\rangle$ and $\langle \hat{x}^2\hat{x}^2(t)\rangle$. Comparing classical Wigner with a classical bath to RPMD for the multidimensional systems, the classical bath calculations tend to be as good as or better than RPMD, apart from the long time values of $\langle \hat{x}^2\hat{x}^2(t)\rangle$.

VI. CONCLUSION

In this article, two versions of a new way of sampling the initial quantum distribution used in the classical Wigner method for the calculation of correlation functions have been presented and tested for the one-dimensional quartic oscillator and double well and a quartic oscillator with linearly coupled harmonic baths. The name used for the new method is Open Polymer Classical Wigner (OPCW).

The new method will always converge toward the exact classical Wigner result as the number of beads in the open polymer necklace goes to infinity. For the y_1-version of the new method and the correlation functions and potentials tested here, this convergence is mostly slow. For some cases, the x_1-version of the new method converges considerably faster.

Compared to FK-LPI, the open polymer sampling for the classical Wigner method can give better, worse, or equal results. The double well potential is a case where the two methods give noticeably different results, with the ones from OPCW being closer to exact classical Wigner. Both methods, however, follow exact quantum mechanics equally well for the double well potential. For a well behaved molecular potential, OPCW will always converge toward the exact classical Wigner result as the calculation gets more refined. A harmonic approximation method such as FK-LPI will not necessarily converge toward the exact classical Wigner result for all potential energy surfaces.

The way forward from this study would be to test the method developed here on other potentials and correlation functions. One set of correlation functions that are of chemical interest and that possibly could be calculated by the presented method are the ones of Miller, Schwartz, and Tromp[43,44] that can be used to acquire reaction rate constants. Potential energy surfaces in reaction rate calculations

tend to have barriers, such as the one in the double well tested here, and this is where the new method may be an improvement over methods such as FK-LPI, since OPCW for the double well approximates the exact classical Wigner result noticeably better than FK-LPI does.

Systems with many degrees of freedom are seen to be computationally demanding. Describing the harmonic baths studied with classical mechanics improves the situation considerably. It would thus be of interest to try this out on other multidimensional systems. This should be particularly useful when the coupling between the system and the bath is weak. It would also be of interest to try a less approximate simplification for the less quantum mechanical degrees of freedom in a system, such as an open polymer equivalent to the ring polymer contraction of Markland and Manolopoulos.[45] Another approach of interest for handling the more computationally demanding systems would be to try to enhance convergence using the techniques recently introduced by Bose and Makri.[12]

ACKNOWLEDGMENTS

Financial support from the Swedish Research Council (Vetenskapsrådet), Diary No. 2016-03275, is acknowledged.

The computations in this work were performed at the Chalmers Centre for Computational Science and Engineering (C3SE), a partner center of the Swedish National Infrastructure for Computing (SNIC).

APPENDIX A: ANALYTIC FORMS OF $A'(y_1, x_2 - x_1)$ FOR $(\hat{A})_W[y_1 p_1]$ BEING A POLYNOMIAL IN p_1

If $(\hat{A})_W[y_1, p_1]$ is a polynomial with respect to p_1, i.e.,

$$(\hat{A})_W[y_1, p_1] = k_n p_1^n + k_{n-1} p_1^{n-1} \ldots k_2 p_1^2 + k_1 p_1 + k_0, \tag{A1}$$

where $k_n, \ldots, k_0$ are constants, then the solution to Eq. (11) is

$$\begin{aligned} A'(y_1, x_2 - x_1) &= \frac{\int_{-\infty}^{\infty} \mathrm{d}p_1 \, (\hat{A})_W[y_1, p_1] \, \mathrm{e}^{-\frac{\beta}{N}\frac{p_1^2}{2m}} \, \mathrm{e}^{-\frac{i}{\hbar} p_1 (x_2 - x_1)}}{\sqrt{\frac{2\pi m N}{\beta}} \, \mathrm{e}^{-\frac{\beta}{N}\frac{mN^2 (x_2 - x_1)^2}{2\hbar^2 \beta^2}}} \\ &= k_n (-i)^n \left(\frac{mN}{2\beta}\right)^{\frac{n}{2}} H_n\left(\sqrt{\frac{mN}{2\beta}}\frac{x_2 - x_1}{\hbar}\right) + k_{n-1}(-i)^{n-1}\left(\frac{mN}{2\beta}\right)^{\frac{n-1}{2}} H_{n-1}\left(\sqrt{\frac{mN}{2\beta}}\frac{x_2 - x_1}{\hbar}\right) \ldots \\ &\quad + k_2 (-i)^2 \left(\frac{mN}{2\beta}\right)^{\frac{2}{2}} H_2\left(\sqrt{\frac{mN}{2\beta}}\frac{x_2 - x_1}{\hbar}\right) + k_1 (-i)\left(\frac{mN}{2\beta}\right)^{\frac{1}{2}} H_1\left(\sqrt{\frac{mN}{2\beta}}\frac{x_2 - x_1}{\hbar}\right) + k_0 \\ &= \sum_{j=0}^{n} k_j (-i)^j \left(\frac{mN}{2\beta}\right)^{\frac{j}{2}} H_j\left(\sqrt{\frac{mN}{2\beta}}\frac{x_2 - x_1}{\hbar}\right), \end{aligned} \tag{A2}$$

where $H_j(\chi)$ is the Hermite polynomial defined by

$$H_j(\chi) = (-1)^j e^{\chi^2} \frac{\mathrm{d}^j}{\mathrm{d}\chi^j} e^{-\chi^2}, \tag{A3}$$

where χ is a dummy variable.

APPENDIX B: KUBO TRANSFORM

One possible form of the Kubo transform[24] of the open polymer expression presented in this article is

$$\begin{aligned} \left\langle \hat{A}\hat{B}(t) \right\rangle_{\mathrm{Kubo}} &= \frac{1}{Z} \mathrm{Tr}\left\{ \frac{1}{\beta} \int_0^{\beta} \mathrm{d}\lambda \, \mathrm{e}^{-\lambda \hat{H}} \hat{A} \, \mathrm{e}^{-(\beta - \lambda)\hat{H}} \hat{B}(t) \right\} \\ &\approx \frac{1}{Z} \left(\frac{mN}{2\pi\beta}\right)^{\frac{N}{2}} \sqrt{\frac{\beta}{2\pi m N}} \hbar^{-N} \left\{ \prod_{j=1}^{N} \int_{-\infty}^{\infty} \mathrm{d}x_j \right\} \int_{-\infty}^{\infty} \mathrm{d}p_N \, \mathrm{e}^{-\frac{i}{\hbar} p_N (x_1 - x_N)} \\ &\quad \times \mathrm{e}^{-\frac{\beta}{N}\left(\frac{p_N^2}{2m} + \sum_{j=1}^{N} V(y_j) + \frac{mN^2}{2\hbar^2\beta^2} \sum_{j=1}^{N-1} (x_{j+1} - x_j)^2\right)} (\hat{B})_W[x(y_N, p_N, t), p(y_N, p_N, t)] \\ &\quad \times \frac{1}{N}\left(\frac{1}{2} A'(y_1, x_2 - x_1) + \sum_{k=1}^{N-2} A'(y_{k+1}, x_{k+2} - x_{k+1}) + \frac{3}{2} A'(y_{N-1}, x_N - x_{N-1}) \right). \end{aligned} \tag{B1}$$

It can be noted that the double counting of $A'(y_{N-1}, x_N - x_{N-1})$ is due to the approximation $\left(\hat{\Omega}\, \mathrm{e}^{-\frac{\beta}{N}\hat{H}}\right)_{\mathrm{W}}[x,p] \approx \left(\hat{\Omega}\right)_{\mathrm{W}}[x,p]\left(\mathrm{e}^{-\frac{\beta}{N}\hat{H}}\right)_{\mathrm{W}}[x,p] \approx \left(\mathrm{e}^{-\frac{\beta}{N}\hat{H}}\hat{\Omega}\right)_{\mathrm{W}}[x,p]$. This double counting leads to an asymmetry that means that the resulting correlation function may have an imaginary part. If using the Kubo transform, this may be an unwanted property, so the mean of the above expression and its complex conjugate may be used instead,

$$\begin{aligned}\left\langle \hat{A}\hat{B}(t)\right\rangle_{\mathrm{Kubo}} \approx{}& \frac{1}{Z}\left(\frac{mN}{2\pi\beta}\right)^{\frac{N}{2}}\sqrt{\frac{\beta}{2\pi mN}}\hbar^{-N}\left\{\prod_{j=1}^{N}\int_{-\infty}^{\infty}\mathrm{d}x_j\right\}\int_{-\infty}^{\infty}\mathrm{d}p_N\ \mathrm{e}^{-\frac{\beta}{N}\left(\frac{p_N^2}{2m}+\sum_{j=1}^{N}V(y_j)+\frac{mN^2}{2\hbar^2\beta^2}\sum_{j=1}^{N-1}(x_{j+1}-x_j)^2\right)}\left(\hat{B}\right)_{\mathrm{W}}[x(y_N,p_N,t),p(y_N,p_N,t)]\\ &\times\frac{1}{2N}\left(\mathrm{e}^{-\frac{i}{\hbar}p_N(x_1-x_N)}\left(\frac{1}{2}A'(y_1,x_2-x_1)+\sum_{k=2}^{N-1}A'(y_k,x_{k+1}-x_k)+\frac{3}{2}A'(y_{N-1},x_N-x_{N-1})\right)\right.\\ &\left.+\,\mathrm{e}^{\frac{i}{\hbar}p_N(x_1-x_N)}\left(\frac{1}{2}A'(y_{N-1},x_{N-1}-x_N)+\sum_{k=1}^{N-2}A'(y_k,x_k-x_{k+1})+\frac{3}{2}A'(y_1,x_1-x_2)\right)\right),\end{aligned}\tag{B2}$$

which should not give an imaginary part. If $A'(y_j, x_{j+1} - x_j)$ is either an even or odd function with regard to $x_{j+1} - x_j$, the expression can be simplified to

$$\begin{aligned}\left\langle \hat{A}\hat{B}(t)\right\rangle_{\mathrm{Kubo,\,even}} \approx{}& \frac{1}{Z}\left(\frac{mN}{2\pi\beta}\right)^{\frac{N}{2}}\sqrt{\frac{\beta}{2\pi mN}}\hbar^{-N}\left\{\prod_{j=1}^{N}\int_{-\infty}^{\infty}\mathrm{d}x_j\right\}\int_{-\infty}^{\infty}\mathrm{d}p_N\ \mathrm{e}^{-\frac{\beta}{N}\left(\frac{p_N^2}{2m}+\sum_{j=1}^{N}V(y_j)+\frac{mN^2}{2\hbar^2\beta^2}\sum_{j=1}^{N-1}(x_{j+1}-x_j)^2\right)}\left(\hat{B}\right)_{\mathrm{W}}[x(y_N,p_N,t),p(y_N,p_N,t)]\\ &\times\frac{1}{N}\left(\cos\left(\frac{p_N(x_1-x_N)}{\hbar}\right)\left(\frac{1}{2}A'(y_1,x_2-x_1)+\sum_{k=2}^{N-2}A'(y_k,x_{k+1}-x_k)+\frac{1}{2}A'(y_{N-1},x_N-x_{N-1})\right)\right.\\ &\left.+\,\mathrm{e}^{\frac{i}{\hbar}p_N(x_1-x_N)}A'(y_1,x_2-x_1)+\mathrm{e}^{-\frac{i}{\hbar}p_N(x_1-x_N)}A'(y_{N-1},x_N-x_{N-1})\right)\end{aligned}\tag{B3}$$

for even A' and

$$\begin{aligned}\left\langle \hat{A}\hat{B}(t)\right\rangle_{\mathrm{Kubo,\,odd}} \approx{}& \frac{1}{Z}\left(\frac{mN}{2\pi\beta}\right)^{\frac{N}{2}}\sqrt{\frac{\beta}{2\pi mN}}\hbar^{-N}\left\{\prod_{j=1}^{N}\int_{-\infty}^{\infty}\mathrm{d}x_j\right\}\int_{-\infty}^{\infty}\mathrm{d}p_N\ \mathrm{e}^{-\frac{\beta}{N}\left(\frac{p_N^2}{2m}+\sum_{j=1}^{N}V(y_j)+\frac{mN^2}{2\hbar^2\beta^2}\sum_{j=1}^{N-1}(x_{j+1}-x_j)^2\right)}\\ &\times\left(\hat{B}\right)_{\mathrm{W}}[x(y_N,p_N,t),p(y_N,p_N,t)]\\ &\times\frac{1}{N}\left(-i\sin\left(\frac{p_N(x_1-x_N)}{\hbar}\right)\left(\frac{1}{2}A'(y_1,x_2-x_1)+\sum_{k=2}^{N-2}A'(y_k,x_{k+1}-x_k)+\frac{1}{2}A'(y_{N-1},x_N-x_{N-1})\right)\right.\\ &\left.-\,\mathrm{e}^{\frac{i}{\hbar}p_N(x_1-x_N)}A'(y_1,x_2-x_1)+\mathrm{e}^{-\frac{i}{\hbar}p_N(x_1-x_N)}A'(y_{N-1},x_N-x_{N-1})\right)\end{aligned}\tag{B4}$$

for odd A'.

APPENDIX C: RESULTS FOR HARMONIC POTENTIAL $\beta\hbar\omega = 8$

Apart from the calculations shown in the main body of this article, the four autocorrelation functions position, position-squared, momentum, and momentum-squared were also calculated for a one-dimensional harmonic oscillator.

The harmonic potential was taken as

$$V_{\mathrm{harmonic}}(x) = \frac{1}{2}m\omega^2x^2,\tag{C1}$$

where ω is the angular frequency of the harmonic oscillation.

The Monte Carlo procedure and molecular dynamics were conducted as for the other systems. The time step used in the molecular dynamics was $0.050\omega^{-1}$.

In order to have exact values to compare our calculated results against, anaytical classical and quantum mechanical correlation functions were used. These functions are collected in Appendix D.

As shown in Fig. 13 for both versions of the new method, the real and imaginary parts of the position autocorrelation function converge from exact classical mechanics toward exact quantum mechanics as the number of beads increases. $\langle \hat{x}\hat{x}(t)\rangle_{x_1}$ converges toward quantum mechanics, with respect to the number of

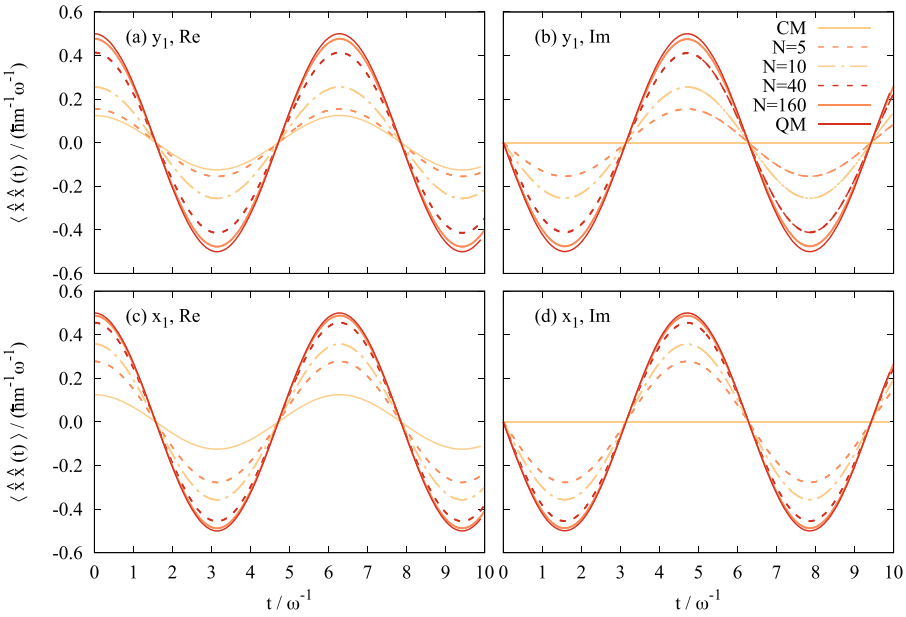

FIG. 13. The position autocorrelation function for a harmonic potential ($\beta\hbar\omega$ = 8). Comparison between different numbers of beads for the two versions of OPCW and exact solutions for classical mechanics (CM) and quantum mechanics (QM). The number of Monte Carlo steps used for each number of beads, N, is 1×10^9 for N = 5, N = 10, and N = 40, and 64×10^9 for N = 160. The standard deviations are in all cases small enough not to be visible. (a) Real part of $\langle \hat{x}\hat{x}(t)\rangle_{y_1}$, (b) imaginary part of $\langle \hat{x}\hat{x}(t)\rangle_{y_1}$, (c) real part of $\langle \hat{x}\hat{x}(t)\rangle_{x_1}$, and (d) imaginary part of $\langle \hat{x}\hat{x}(t)\rangle_{x_1}$.

beads, noticeably faster than $\langle \hat{x}\hat{x}(t)\rangle_{y_1}$. This ordering of speed of convergence with regard to the number of beads, N, is what could be expected since $\langle \hat{x}\hat{x}(t)\rangle_{x_1}$ requires the positions of neighboring beads to converge to the same value, while $\langle \hat{x}\hat{x}(t)\rangle_{y_1}$ also requires the positions of next neighboring beads to converge to the same value (see Appendix E 1).

In Fig. 14, the position-squared autocorrelation function can be seen for both versions of the method studied. Both versions of the method, just as for the previous correlation function, converge from classical toward quantum mechanics as the number of beads increases. Similar to the previous correlation function, $\langle \hat{x}^2\hat{x}^2(t)\rangle_{x_1}$ converges faster with respect to the number of beads than $\langle \hat{x}^2\hat{x}^2(t)\rangle_{y_1}$, as could be expected (see Appendix E 2).

In Fig. 15, the position and position-squared autocorrelation functions from the two versions of the open polymer method can be compared to each other, exact classical mechanics, exact quantum mechanics, and RPMD. FK-LPI is always exact for a harmonic potential, so it is equivalent to exact quantum mechanics. As RPMD is exact for correlation functions with at least one linear operator in a harmonic potential,[3] the exact RPMD result is also equivalent

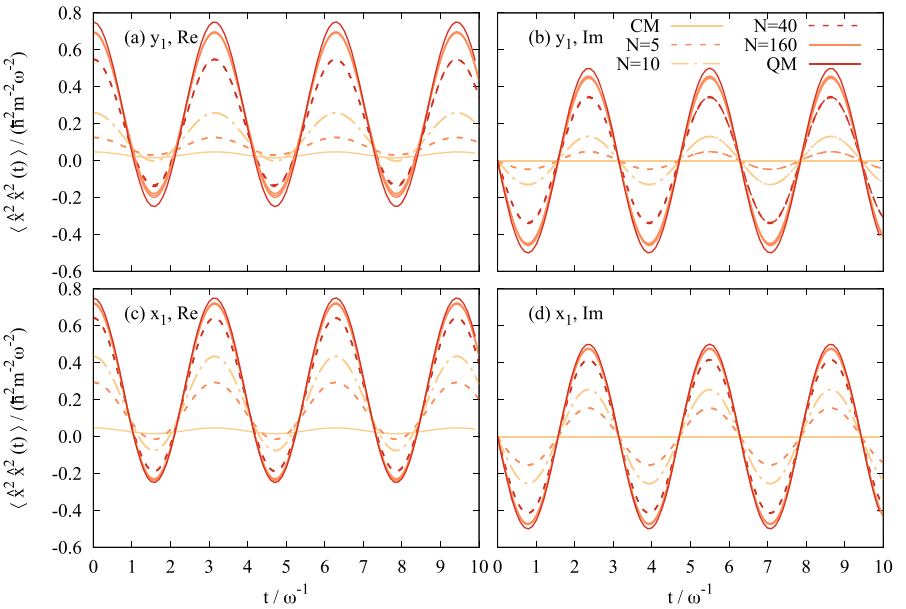

FIG. 14. The position-squared autocorrelation function for a harmonic potential ($\beta\hbar\omega$ = 8). Comparison between different numbers of beads for the two versions of OPCW and exact solutions for classical mechanics (CM) and quantum mechanics (QM). The number of Monte Carlo steps used for each number of beads, N, is 1×10^9 for N = 5 and N = 10, 4×10^9 for N = 40, and 64×10^9 for N = 160. The outer lines of each type show the standard deviations for the results. If the standard deviation is small enough, the outer lines are not visible. (a) Real part of $\langle \hat{x}^2\hat{x}^2(t)\rangle_{y_1}$, (b) imaginary part of $\langle \hat{x}^2\hat{x}^2(t)\rangle_{y_1}$, (c) real part of $\langle \hat{x}^2\hat{x}^2(t)\rangle_{x_1}$, and (d) imaginary part of $\langle \hat{x}^2\hat{x}^2(t)\rangle_{x_1}$.

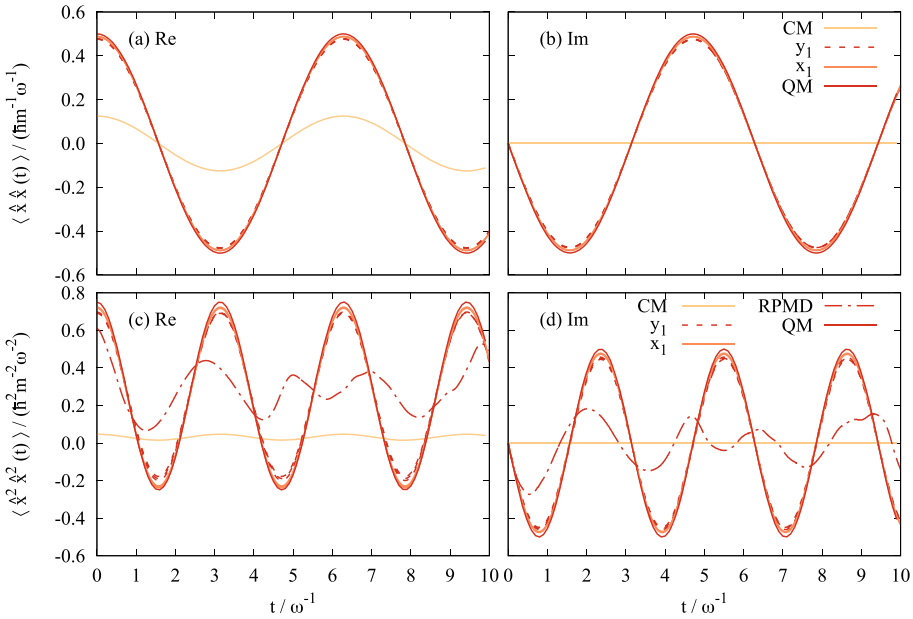

FIG. 15. The position and position-squared autocorrelation functions for a harmonic potential ($\beta\hbar\omega$ = 8). Comparison between the two versions of OPCW and numerically exact solutions for classical mechanics (CM), classical Wigner (CW), RPMD, and quantum mechanics (QM). The number of beads used in the y_1- and x_1-calculations is N = 160, and the number of Monte Carlo steps is 64 × 10^9. The outer lines of each type show the standard deviations for the results. If the standard deviation is small enough, the outer lines are not visible. (a) Real part of $\langle\hat{x}\hat{x}(t)\rangle$, (b) imaginary part of $\langle\hat{x}\hat{x}(t)\rangle$, (c) real part of $\langle\hat{x}^2\hat{x}^2(t)\rangle$, and (d) imaginary part of $\langle\hat{x}^2\hat{x}^2(t)\rangle$.

to exact quantum mechanics for $\langle\hat{x}\hat{x}(t)\rangle$. For $\langle\hat{x}^2\hat{x}^2(t)\rangle$, it can be seen that the classical Wigner method gives better results than RPMD. This is to be expected as the classical Wigner method is exact for any correlation function for a harmonic potential, while RPMD is not exact when both operators in the correlation function are non-linear.

In Fig. 16, the momentum and momentum-squared autocorrelation functions are shown. For these correlation functions, the

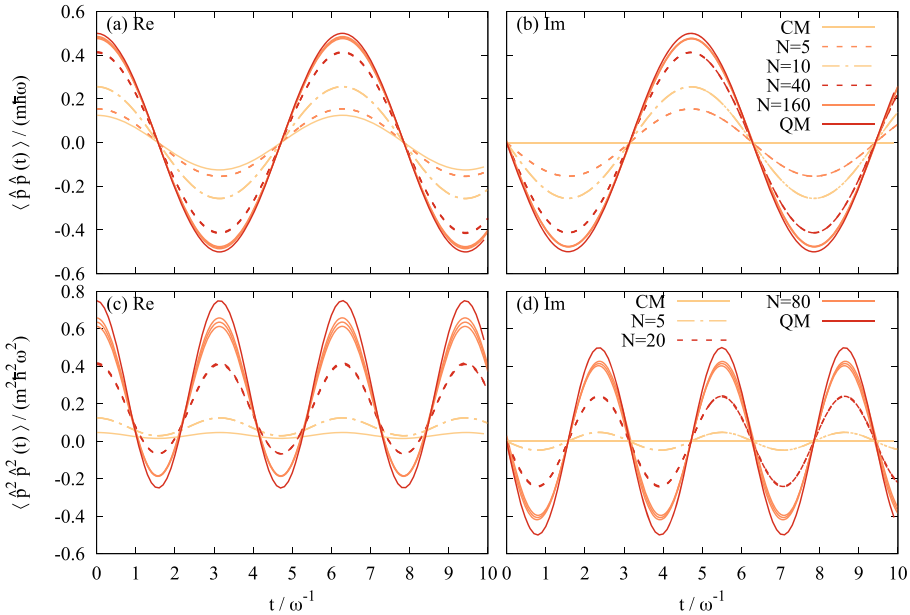

FIG. 16. The momentum and momentum-squared autocorrelation functions for a harmonic potential ($\beta\hbar\omega$ = 8). Comparison between different numbers of beads for OPCW [with $\langle\hat{p}\hat{p}(t)\rangle_{y_1}$ and $\langle\hat{p}^2\hat{p}^2(t)\rangle_{y_1}$ being identical to $\langle\hat{p}\hat{p}(t)\rangle_{x_1}$ and $\langle\hat{p}^2\hat{p}^2(t)\rangle_{x_1}$, respectively] and exact solutions for classical mechanics (CM) and quantum mechanics (QM). The number of Monte Carlo steps used for each number of beads, N, for the calculation of $\langle\hat{p}\hat{p}(t)\rangle_{y_1,x_1}$ is 1 × 10^9 for N = 5 and N = 10, 4 × 10^9 for N = 40, and 64 × 10^9 for N = 160. The number of Monte Carlo steps used for each number of beads for the calculation of $\langle\hat{p}^2\hat{p}^2(t)\rangle_{y_1,x_1}$ is 1 × 10^9 for N = 5, 4 × 10^9 for N = 20, and 128 × 10^9 for N = 80. The outer lines of each type show the standard deviations for the results. If the standard deviation is small enough, the outer lines are not visible. (a) Real part of $\langle\hat{p}\hat{p}(t)\rangle_{y_1,x_1}$, (b) imaginary part of $\langle\hat{p}\hat{p}(t)\rangle_{y_1,x_1}$, (c) real part of $\langle\hat{p}^2\hat{p}^2(t)\rangle_{y_1,x_1}$, and (d) imaginary part of $\langle\hat{p}^2\hat{p}^2(t)\rangle_{y_1,x_1}$.

two versions of the method are identical. $\langle \hat{p}\hat{p}(t)\rangle_{y_1,x_1}$ converges in a similar way as $\langle \hat{x}\hat{x}(t)\rangle_{y_1}$ does with respect to the number of beads. $\langle \hat{p}^2\hat{p}^2(t)\rangle_{y_1,x_1}$, as all the other correlation functions, converges with respect to the number of beads from classical toward quantum mechanics. In this work, $\langle \hat{p}^2\hat{p}^2(t)\rangle_{y_1,x_1}$ is the most difficult correlation function to converge with respect to the number of Monte Carlo steps. That is why no results from calculations with $N = 160$ are shown, and why the standard deviations are visible in the results for $N = 80$.

APPENDIX D: ANALYTIC CORRELATION FUNCTIONS FOR THE HARMONIC OSCILLATOR

For the harmonic oscillator described in Appendix C, correlation functions can be calculated analytically. $\langle \hat{x}\hat{x}(t)\rangle$ and $\langle \hat{p}\hat{p}(t)\rangle$ are straightforward to derive. $\langle \hat{x}^2\hat{x}^2(t)\rangle$ and $\langle \hat{p}^2\hat{p}^2(t)\rangle$ can be acquired from the simpler correlation functions by using the cumulant expansion of Cao and Voth.[46] The correlation functions are, for classical mechanics,

$$\langle \hat{x}\hat{x}(t)\rangle = \frac{1}{\beta m\omega^2}\cos(\omega t), \tag{D1}$$

$$\langle \hat{x}^2\hat{x}^2(t)\rangle = \frac{1}{\beta^2 m^2\omega^4}\left(1+2\cos^2(\omega t)\right), \tag{D2}$$

$$\langle \hat{p}\hat{p}(t)\rangle = \frac{m}{\beta}\cos(\omega t), \tag{D3}$$

$$\langle \hat{p}^2\hat{p}^2(t)\rangle = \frac{m^2}{\beta^2}\left(1+2\cos^2(\omega t)\right), \tag{D4}$$

and, for quantum mechanics,

$$\langle \hat{x}\hat{x}(t)\rangle = \frac{\hbar}{2\,m\omega}\left(\frac{e^{\beta\hbar\omega}}{e^{\beta\hbar\omega}-1}e^{-i\omega t}+\frac{1}{e^{\beta\hbar\omega}-1}e^{i\omega t}\right), \tag{D5}$$

$$\langle \hat{x}^2\hat{x}^2(t)\rangle = \frac{\hbar^2}{4\,m^2\omega^2}\left(\left(\frac{e^{\beta\hbar\omega}+1}{e^{\beta\hbar\omega}-1}\right)^2 + 2\left(\frac{e^{\beta\hbar\omega}}{e^{\beta\hbar\omega}-1}e^{-i\omega t}+\frac{1}{e^{\beta\hbar\omega}-1}e^{i\omega t}\right)^2\right), \tag{D6}$$

$$\langle \hat{p}\hat{p}(t)\rangle = \frac{m\hbar\omega}{2}\left(\frac{e^{\beta\hbar\omega}}{e^{\beta\hbar\omega}-1}e^{-i\omega t}+\frac{1}{e^{\beta\hbar\omega}-1}e^{i\omega t}\right), \tag{D7}$$

$$\langle \hat{p}^2\hat{p}^2(t)\rangle = \frac{m^2\hbar^2\omega^2}{4}\left(\left(\frac{e^{\beta\hbar\omega}+1}{e^{\beta\hbar\omega}-1}\right)^2 + 2\left(\frac{e^{\beta\hbar\omega}}{e^{\beta\hbar\omega}-1}e^{-i\omega t}+\frac{1}{e^{\beta\hbar\omega}-1}e^{i\omega t}\right)^2\right). \tag{D8}$$

APPENDIX E: COMPARISON OF THE REAL AND IMAGINARY PARTS OF CORRELATION FUNCTIONS FOR THE HARMONIC POTENTIAL

For the harmonic oscillator, the analytical equations of motion can be put into $\left(\hat{B}\right)_{\mathrm{W}}[x(y_N,p_N,t),p(y_N,p_N,t)]$ and $\left(\hat{B}\right)_{\mathrm{W}}[x(x_N,p_N,t),p(x_N,p_N,t)]$ in Eqs. (12) and (13). This appendix shows how some autocorrelation functions behave for the two versions of the method presented in this paper.

1. Position autocorrelation function, $\langle \hat{x}\hat{x}(t)\rangle$

For the case of $\langle \hat{x}\hat{x}(t)\rangle$, entering the analytical equations of motion into Eqs. (12) and (13) leads to

$$\begin{aligned}\langle \hat{x}\hat{x}(t)\rangle_{y_1} = {}& \frac{1}{Z}\left(\frac{mN}{2\pi\beta}\right)^{\frac{N}{2}}\sqrt{\frac{\beta}{2\pi mN}}\hbar^{-N}\left\{\prod_{j=1}^{N}\int_{-\infty}^{\infty}dx_j\right\}\\ &\times\int_{-\infty}^{\infty}dp_N\, e^{-\frac{i}{\hbar}p_N(x_1-x_N)}\\ &\times e^{-\frac{\beta}{N}\left(\frac{p_N^2}{2m}+\sum_{j=1}^{N}V(y_j)+\frac{mN^2}{2\hbar^2\beta^2}\sum_{j=1}^{N-1}(x_{j+1}-x_j)^2\right)}\\ &\times y_1\left(y_N\cos(\omega t)+\frac{p_N}{m\omega}\sin(\omega t)\right),\end{aligned} \tag{E1}$$

$$\begin{aligned}\langle \hat{x}\hat{x}(t)\rangle_{x_1} = {}& \frac{1}{Z}\left(\frac{mN}{2\pi\beta}\right)^{\frac{N}{2}}\sqrt{\frac{\beta}{2\pi mN}}\hbar^{-N}\left\{\prod_{j=1}^{N}\int_{-\infty}^{\infty}dx_j\right\}\\ &\times\int_{-\infty}^{\infty}dp_N\, e^{-\frac{i}{\hbar}p_N(x_1-x_N)}\\ &\times e^{-\frac{\beta}{N}\left(\frac{p_N^2}{2m}+\sum_{j=1}^{N}V(y_j)+\frac{mN^2}{2\hbar^2\beta^2}\sum_{j=1}^{N-1}(x_{j+1}-x_j)^2\right)}\\ &\times x_1\left(y_N\cos(\omega t)+\frac{p_N}{m\omega}\sin(\omega t)\right).\end{aligned} \tag{E2}$$

To simplify, p_N can be integrated out and all constants that are identical in both cases can be collected into a single constant, C,

$$\begin{aligned}\langle \hat{x}\hat{x}(t)\rangle_{y_1} = {}& C\left\{\prod_{j=1}^{N}\int_{-\infty}^{\infty}dx_j\right\}e^{-\frac{\beta}{N}\left(\sum_{j=1}^{N}V(y_j)+\frac{mN^2}{2\hbar^2\beta^2}\sum_{j=1}^{N}(x_{j+1}-x_j)^2\right)}\\ &\times y_1\left(y_N\cos(\omega t)-\frac{iN}{\beta\hbar\omega}(x_1-x_N)\sin(\omega t)\right),\end{aligned} \tag{E3}$$

$$\begin{aligned}\langle \hat{x}\hat{x}(t)\rangle_{x_1} = {}& C\left\{\prod_{j=1}^{N}\int_{-\infty}^{\infty}dx_j\right\}e^{-\frac{\beta}{N}\left(\sum_{j=1}^{N}V(y_j)+\frac{mN^2}{2\hbar^2\beta^2}\sum_{j=1}^{N}(x_{j+1}-x_j)^2\right)}\\ &\times x_1\left(y_N\cos(\omega t)-\frac{iN}{\beta\hbar\omega}(x_1-x_N)\sin(\omega t)\right).\end{aligned} \tag{E4}$$

These correlation functions are Boltzmann-weighted averages, which can be simplified to

$$\langle \hat{x}\hat{x}(t)\rangle_{y_1} = \left\langle y_1\left(y_N\cos(\omega t)-\frac{iN}{\beta\hbar\omega}(x_1-x_N)\sin(\omega t)\right)\right\rangle, \tag{E5}$$

$$\langle \hat{x}\hat{x}(t)\rangle_{x_1} = \left\langle x_1\left(y_N\cos(\omega t)-\frac{iN}{\beta\hbar\omega}(x_1-x_N)\sin(\omega t)\right)\right\rangle. \tag{E6}$$

Now, the correlation functions can be separated into the real parts,

$$\begin{aligned}\mathrm{Re}\langle \hat{x}\hat{x}(t)\rangle_{y_1} &= \cos(\omega t)\langle y_1y_N\rangle\\ &= \frac{\cos(\omega t)}{4}\left(\langle x_1^2\rangle+\langle x_1x_N\rangle+\langle x_1x_2\rangle+\langle x_2x_N\rangle\right)\\ &= \frac{\cos(\omega t)}{4}\left(\langle x_1^2\rangle+2\langle x_1x_N\rangle+\langle x_2x_N\rangle\right),\end{aligned} \tag{E7}$$

$$\mathrm{Re}\langle\hat{x}\hat{x}(t)\rangle_{x_1} = \cos(\omega t)\langle x_1 y_N\rangle = \frac{\cos(\omega t)}{2}\left(\langle x_1^2\rangle + \langle x_1 x_N\rangle\right), \tag{E8}$$

and the imaginary parts,

$$\begin{aligned}\mathrm{Im}\langle\hat{x}\hat{x}(t)\rangle_{y_1} &= -\frac{N}{\beta\hbar\omega}\sin(\omega t)\langle y_1(x_1 - x_N)\rangle \\ &= -\frac{N}{2\beta\hbar\omega}\sin(\omega t)\left(\langle x_1^2\rangle + \langle x_1 x_2\rangle - \langle x_1 x_N\rangle - \langle x_2 x_N\rangle\right) \\ &= -\frac{N}{2\beta\hbar\omega}\sin(\omega t)\left(\langle x_1^2\rangle - \langle x_2 x_N\rangle\right), \end{aligned} \tag{E9}$$

$$\begin{aligned}\mathrm{Im}\langle\hat{x}\hat{x}(t)\rangle_{x_1} &= -\frac{N}{\beta\hbar\omega}\sin(\omega t)\langle x_1(x_1 - x_N)\rangle \\ &= -\frac{N}{\beta\hbar\omega}\sin(\omega t)\left(\langle x_1^2\rangle - \langle x_1 x_N\rangle\right), \end{aligned} \tag{E10}$$

where it has been used that all beads are equivalent after the last momentum was integrated out, so, e.g., $\langle x_N^2\rangle = \langle x_1^2\rangle$ and $\langle x_1 x_N\rangle = \langle x_1 x_2\rangle$.

For the real part, $\langle x_1^2\rangle\cos(\omega t)$ is the exact quantum mechanics, apart from that the Boltzmann weighting factor in the average is approximate as long as N is finite. $\mathrm{Re}\langle\hat{x}\hat{x}(t)\rangle_{x_1}$ consists to a larger degree of $\langle x_1^2\rangle\cos(\omega t)$ than $\mathrm{Re}\langle\hat{x}\hat{x}(t)\rangle_{y_1}$ does. When $N \to \infty$ and the distance between beads becomes smaller both $\langle x_1 x_N\rangle$ and $\langle x_2 x_N\rangle$ will converge toward $\langle x_1^2\rangle$. $\langle x_2 x_N\rangle$ will most likely converge more slowly than $\langle x_1 x_N\rangle$ as it depends on next neighboring beads instead of immediately neighboring beads. This means that $\mathrm{Re}\langle\hat{x}\hat{x}(t)\rangle_{x_1}$ could be expected to convergence toward exact quantum mechanics faster than $\mathrm{Re}\langle\hat{x}\hat{x}(t)\rangle_{y_1}$ with respect to the number of beads. With the same kind of reasoning, $\mathrm{Im}\langle\hat{x}\hat{x}(t)\rangle_{x_1}$ could be expected to converge faster with respect to the number of beads than $\mathrm{Im}\langle\hat{x}\hat{x}(t)\rangle_{y_1}$, since the former depends on $\langle x_1 x_N\rangle$ and the latter depends on $\langle x_2 x_N\rangle$.

2. Comparison of real and imaginary parts of $\langle\hat{x}^2\hat{x}^2(t)\rangle$ for the harmonic potential

For $\langle\hat{x}^2\hat{x}^2(t)\rangle$, the equivalent of Eqs. (E5) and (E6) is

$$\langle\hat{x}^2\hat{x}^2(t)\rangle_{y_1} = \left\langle y_1^2\left(y_N^2\cos^2(\omega t) - \frac{iN}{\beta\hbar\omega}(x_1 - x_N)y_N\sin(\omega t)\cos(\omega t) - \frac{N^2}{\beta^2\hbar^2\omega^2}(x_1 - x_N)^2\sin^2(\omega t) + \frac{N}{\beta\omega^2 m}\sin^2(\omega t)\right)\right\rangle, \tag{E11}$$

$$\langle\hat{x}^2\hat{x}^2(t)\rangle_{x_1} = \left\langle x_1^2\left(y_N^2\cos^2(\omega t) - \frac{iN}{\beta\hbar\omega}(x_1 - x_N)y_N\sin(\omega t)\cos(\omega t) - \frac{N^2}{\beta^2\hbar^2\omega^2}(x_1 - x_N)^2\sin^2(\omega t) + \frac{N}{\beta\omega^2 m}\sin^2(\omega t)\right)\right\rangle. \tag{E12}$$

Separating into real parts

$$\begin{aligned}\mathrm{Re}\langle\hat{x}^2\hat{x}^2(t)\rangle_{y_1} &= \left\langle y_1^2 y_N^2\cos^2(\omega t) - y_1^2\frac{N^2}{\beta^2\hbar^2\omega^2}(x_1 - x_N)^2\sin^2(\omega t) + y_1^2\frac{N}{\beta\omega^2 m}\sin^2(\omega t)\right\rangle \\ &= \frac{\cos^2(\omega t)}{16}\left\langle x_1^4 + 2x_1^3x_2 + 2x_1^3x_N + x_1^2x_2^2 + 4x_1^2x_2x_N + x_1^2x_N^2 + 2x_1x_2^2x_N + 2x_1x_2x_N^2 + x_2^2x_N^2\right\rangle \\ &\quad - \frac{N^2\sin^2(\omega t)}{4\beta^2\hbar^2\omega^2}\left\langle x_1^4 + 2x_1^3x_2 - 2x_1^3x_N + x_1^2x_2^2 - 4x_1^2x_2x_N + x_1^2x_N^2 - 2x_1x_2^2x_N + 2x_1x_2x_N^2 + x_2^2x_N^2\right\rangle \\ &\quad + \frac{N\sin^2(\omega t)}{4\beta\omega^2 m}\left\langle x_1^2 + 2x_1x_2 + x_2^2\right\rangle \\ &= \frac{\cos^2(\omega t)}{16}\left(\langle x_1^4\rangle + 4\langle x_1^3x_N\rangle + 2\langle x_1^2x_N^2\rangle + 4\langle x_1^2x_2x_N\rangle + 4\langle x_1x_2x_N^2\rangle + \langle x_2^2x_N^2\rangle\right) \\ &\quad - \frac{N^2\sin^2(\omega t)}{4\beta^2\hbar^2\omega^2}\left(\langle x_1^4\rangle + 2\langle x_1^2x_N^2\rangle - 4\langle x_1^2x_2x_N\rangle + \langle x_2^2x_N^2\rangle\right) + \frac{N\sin^2(\omega t)}{2\beta\omega^2 m}\left(\langle x_1^2\rangle + \langle x_1x_N\rangle\right), \end{aligned} \tag{E13}$$

$$\begin{aligned}\mathrm{Re}\langle\hat{x}^2\hat{x}^2(t)\rangle_{x_1} &= \left\langle x_1^2 y_N^2\cos^2(\omega t) - x_1^2\frac{N^2}{\beta^2\hbar^2\omega^2}(x_1 - x_N)^2\sin^2(\omega t) + x_1^2\frac{N}{\beta\omega^2 m}\sin^2(\omega t)\right\rangle \\ &= \frac{\cos^2(\omega t)}{4}\left(\langle x_1^4\rangle + 2\langle x_1^3x_N\rangle + \langle x_1^2x_N^2\rangle\right) - \frac{N^2\sin^2(\omega t)}{\beta^2\hbar^2\omega^2}\left(\langle x_1^4\rangle - 2\langle x_1^3x_N\rangle + \langle x_1^2x_N^2\rangle\right) + \frac{N\sin^2(\omega t)}{\beta\omega^2 m}\langle x_1^2\rangle \end{aligned} \tag{E14}$$

and imaginary parts

$$\begin{aligned}\mathrm{Im}\left\langle \hat{x}^2\hat{x}^2(t)\right\rangle_{y_1} &= -\frac{N}{\beta\hbar\omega}\sin(\omega t)\cos(\omega t)\left\langle y_1^2(x_1-x_N)y_N\right\rangle \\ &= -\frac{N}{8\beta\hbar\omega}\sin(\omega t)\cos(\omega t)\Big(\left\langle x_1^4\right\rangle + 2\left\langle x_1^3x_2\right\rangle \\ &\quad + \left\langle x_1^2x_2^2\right\rangle - \left\langle x_1^2x_N^2\right\rangle - 2\left\langle x_1x_2x_N^2\right\rangle - \left\langle x_2^2x_N^2\right\rangle\Big) \\ &= -\frac{N}{8\beta\hbar\omega}\sin(\omega t)\cos(\omega t)\Big(\left\langle x_1^4\right\rangle + 2\left\langle x_1^3x_2\right\rangle \\ &\quad - 2\left\langle x_1x_2x_N^2\right\rangle - \left\langle x_2^2x_N^2\right\rangle\Big), \end{aligned} \tag{E15}$$

$$\begin{aligned}\mathrm{Im}\left\langle \hat{x}^2\hat{x}^2(t)\right\rangle_{x_1} &= -\frac{N}{\beta\hbar\omega}\sin(\omega t)\cos(\omega t)\left\langle x_1^2(x_1-x_N)y_N\right\rangle \\ &= -\frac{N}{2\beta\hbar\omega}\sin(\omega t)\cos(\omega t)\Big(\left\langle x_1^4\right\rangle - \left\langle x_1^2x_N^2\right\rangle\Big). \end{aligned} \tag{E16}$$

From these expressions, it can be seen that $\left\langle \hat{x}^2\hat{x}^2(t)\right\rangle_{x_1}$ for both the real and imaginary parts is a combination of fewer and less complex averages than $\left\langle \hat{x}^2\hat{x}^2(t)\right\rangle_{y_1}$. Less complex in this case means averages of fewer different positions and of positions closer to each other. Thus, it can be expected that $\left\langle \hat{x}^2\hat{x}^2(t)\right\rangle_{x_1}$ converges faster with regard to the number of beads than $\left\langle \hat{x}^2\hat{x}^2(t)\right\rangle_{y_1}$ does.

REFERENCES

[1] J. Cao and G. A. Voth, J. Chem. Phys. **99**, 10070 (1993).
[2] S. Jang and G. A. Voth, J. Chem. Phys. **111**, 2357 (1999).
[3] I. R. Craig and D. E. Manolopoulos, J. Chem. Phys. **121**, 3368 (2004).
[4] W. H. Miller, J. Chem. Phys. **53**, 3578 (1970).
[5] W. H. Miller, J. Phys. Chem. A **105**, 2942 (2001).
[6] T. J. H. Hele, M. J. Willatt, A. Muolo, and S. C. Althorpe, J. Chem. Phys. **142**, 134103 (2015).
[7] E. J. Heller, J. Chem. Phys. **65**, 1289 (1976).
[8] H. Wang, X. Sun, and W. H. Miller, J. Chem. Phys. **108**, 9726 (1998).
[9] T. J. H. Hele, M. J. Willatt, A. Muolo, and S. C. Althorpe, J. Chem. Phys. **142**, 191101 (2015).
[10] D. R. Reichman, P.-N. Roy, S. Jang, and G. A. Voth, J. Chem. Phys. **113**, 919 (2000).
[11] X. Sun, H. Wang, and W. H. Miller, J. Chem. Phys. **109**, 4190 (1998).
[12] A. Bose and N. Makri, J. Phys. Chem. A **123**, 4284 (2019).
[13] S. Bonella, M. Monteferrante, C. Pierleoni, and G. Ciccotti, J. Chem. Phys. **133**, 164105 (2010).
[14] S. Bonella and G. Ciccotti, Entropy **16**, 86 (2013).
[15] E. Wigner, Phys. Rev. **40**, 749 (1932).
[16] J. E. Moyal, Math. Proc. Cambridge Philos. Soc. **45**, 99 (1949).
[17] J. Liu, Int. J. Quant. Chem. **115**, 657 (2015).
[18] J. A. Poulsen, J. Scheers, G. Nyman, and P. J. Rossky, Phys. Rev. B **75**, 224505 (2007).
[19] Q. Shi and E. Geva, J. Phys. Chem. A **107**, 9059 (2003).
[20] Q. Shi and E. Geva, J. Phys. Chem. A **107**, 9070 (2003).
[21] S. Habershon and D. E. Manolopoulos, J. Chem. Phys. **131**, 244518 (2009).
[22] N. Marković and J. A. Poulsen, J. Phys. Chem. A **112**, 1701 (2008).
[23] R. P. Feynman and A. R. Hibbs, *Quantum Mechanics and Path Integrals* (McGraw-Hill Companies, Inc., New York, 1965).
[24] R. Kubo, J. Phys. Soc. Jpn. **12**, 570 (1957).
[25] M. Parrinello and A. Rahman, J. Chem. Phys. **80**, 860 (1984).
[26] J. A. Barker, J. Chem. Phys. **70**, 2914 (1979).
[27] J. R. Cendagorta, Z. Bačić, and M. E. Tuckerman, J. Chem. Phys. **148**, 102340 (2018).
[28] A. O. Caldeira and A. J. Leggett, Ann. Phys. **149**, 374 (1983).
[29] I. R. Craig and D. E. Manolopoulos, J. Chem. Phys. **122**, 084106 (2005).
[30] M. P. Allen and D. J. Tildesley, *Computer Simulation of Liquids* (Oxford University Press, Oxford, UK, 1987).
[31] W. H. Press, S. A. Teukolsky, W. T. Vetterling, and B. P. Flannery, *Numerical Recipes in FORTRAN: The Art of Scientific Computing*, 2nd ed. (Cambridge University Press, Cambridge, UK, 1992).
[32] L. Verlet, Phys. Rev. **159**, 98 (1967).
[33] W. C. Swope, H. C. Andersen, P. H. Berens, and K. R. Wilson, J. Chem. Phys. **76**, 637 (1982).
[34] R. Friedberg and J. E. Cameron, J. Chem. Phys. **52**, 6049 (1970).
[35] J. M. Flegal, M. Haran, and G. L. Jones, Stat. Sci. **23**, 250 (2008).
[36] D. Thirumalai, E. J. Bruskin, and B. J. Berne, J. Chem. Phys. **79**, 5063 (1983).
[37] J. A. Poulsen, G. Nyman, and P. J. Rossky, J. Chem. Phys. **119**, 12179 (2003).
[38] J. Liu and W. H. Miller, J. Chem. Phys. **125**, 224104 (2006).
[39] J. Liu and W. H. Miller, J. Chem. Phys. **131**, 074113 (2009).
[40] R. P. Feynman and H. Kleinert, Phys. Rev. A **34**, 5080 (1986).
[41] B. J. Braams, T. F. Miller, and D. E. Manolopoulos, Chem. Phys. Lett. **418**, 179 (2006).
[42] T. F. Miller and D. E. Manolopoulos, J. Chem. Phys. **122**, 184503 (2005).
[43] W. H. Miller, S. D. Schwartz, and J. W. Tromp, J. Chem. Phys. **79**, 4889 (1983).
[44] W. H. Miller, J. Chem. Phys. **61**, 1823 (1974).
[45] T. E. Markland and D. E. Manolopoulos, J. Chem. Phys. **129**, 024105 (2008).
[46] J. Cao and G. A. Voth, J. Chem. Phys. **100**, 5106 (1994).